広島大学学術情報リポジトリ
Hiroshima University Institutional Repository

Title	The Uncertainty of Local Flow Parameters During Inundation Flow Over Complex Topographies with Elevation Errors
Auther(s)	Tsubaki, Ryota; Kawahara, Yoshihisa
Citation	Journal of Hydrology , 486 : 71 - 87
Issue Date	2013-04-12
DOI	10.1016/j.jhydrol.2013.01.042
Self DOI	
URL	http://ir.lib.hiroshima-u.ac.jp/00038852
Right	Copyright (c) 2013 Elsevier B.V. All rights reserved.
Relation	

11

The Uncertainty of Local Flow Parameters During Inundation Flow

Over Complex Topographies with Elevation Errors

by

Ryota Tsubaki[*1] and Yoshihisa Kawahara[1]

* Corresponding author, Phone/Fax 81-82-424-7847, Mail rtsubaki@hiroshima-u.ac.jp

1 Department of Civil and Environmental Engineering, Hiroshima University,

1-4-1 Kagamiyama, Higashi-hiroshima, 739-8527, Japan

Abstract

Since the topographical data obtained from LiDAR (Light Detection and Ranging) measurements is superior in resolution and accuracy as compared to conventional geospatial data, over the last decade aerial LiDAR (Light Detection and Ranging) has been widely used for obtaining geospatial information. However, digital terrain models made from LiDAR data retain some degree of uncertainty as a result of the measurement principles and the operational limitations of LiDAR surveying. LiDAR cannot precisely measure topographical elements such as ground undulation covered by vegetation, curbstones, etc. Such instrumental and physical uncertainties may impact an estimated result in an inundation flow simulation. Meanwhile, how much and how these topographical uncertainties affect calculated results is not understood. To evaluate the effect of topographical uncertainty on the calculated inundation flow, three representative terrains were prepared that included errors in elevation. Here, the topographical uncertainty that was introduced was generated using a fractal algorithm in order to represent the spatial structure of the elevation uncertainty. Then, inundation flows over model terrains were calculated with an unstructured finite volume flow model that solved shallow water equations. The sensitivity of the elevation uncertainty on the calculated inundated propagation, especially the local flow velocity, was evaluated. The predictability of inundation flow over complex topography is discussed, as well as its relationship to topographical features.

Keywords: inundation simulation, complex topography, LiDAR, shallow water flow model, LIC, water level profile.

1. Introduction

46 Aerial LiDAR (Light Detection and Ranging) measurements have been widely used for obtaining

47 topographical data. LiDAR measurements allow one to survey the distribution of ground surface

48 elevation (e.g. Bates, 2003) and the bathymetry under water surfaces (McKean et al., 2009). Spatial

49 resolution and elevation accuracy are greatly enhanced as compared to conventional surveying

50 methods. As compared with aerial LiDAR, terrestrial LiDAR is also a powerful tool for obtaining

51 complex geometry using a higher density and accuracy.

52 Numerical flow simulations have achieved great strides in solving flow equations stably and

53 accurately (Alcrude and Garcia-Navarro, 1993; Anastasiou and Chan, 1997; Caleffi et al., 2003).

54 The development of computational speed and the popularization of an efficient coding technique

55 (e.g. OpenMP (Open MultiProcessing) or MPI (Message Passing Interface)) enabled us to conduct

56 detailed and realistic inundation flow simulations using accurate flow models and high-resolution

57 calculation grids that were based on detailed topographical data (Cobby et al., 2003; Soares-Frazão

58 et al., 2008; Schubert et al., 2008; Neal et al., 2010; and Sanders et al., 2010).

59 LiDAR is a high-resolution and accurate method for obtaining topographical data (Néelz et al., 2006;

60 Mason et al., 2007), even though the spatial resolution and the elevation accuracy have restrictions

61 as a result of operational and device limitations. Typically, since aerial LiDAR detects the ground

62 surface from the sky, elevations of ground surfaces under vegetation cover or buildings cannot be

63 measured directly (Figure 1). Also difficult is precisely measuring small-scale topographical

64 elements such as planted vegetation on roadsides, and the distribution of parked cars and curbstones

65 that have some impact on inundation flows (Bales and Wagner, 2009, Mignot et al., 2006). The

66 LiDAR survey provides massive numbers of data points (point cloud; Sithole and Vosselman 2004),

67 then the digital terrain models is generated by the spatial reconstruction of LiDAR point data. In the

68 area close to buildings or under the elevated road, laser from sky is unable to reach to the ground

69 surface. In the ground surface covered by vegetation, some laser pulse is able to arrive to the ground

70 but the point density of true ground returns is drastically reduced due to leaf interference. Due to

71 these limitations, digital terrain models made from LiDAR data result in non-negligible uncertainty,

72 and, in turn, impact the predicted behavior of inundation flow (e.g. impact of elevated road is

73 discussed in Abdullah et al. 2011). The effects of uncertainties for inflow and roughness parameters

74 were explored in Schumann et al. (2008), Pappenberger et al. (2009), and Bales and Wagner (2009).

75 The uncertainties for inflow have been estimated and the range has been gradually reduced based on

76 advancements in hydrological modeling (e.g. Shamseldin, 1997; Chuntian et al., 2002; Wagener et

77 al., 2003; Wu et al., 2009). The effect and the parameterization of the roughness coefficient within

78 the flood plain were a classical key point in the inundation flow simulation; and within a number of

79 references discussed on this point (e.g. Neal et al., 2009; Casas et al., 2010; and Stephens et al.,

80 2012). On the other hand, the effect of elevation uncertainty on the predicted flow is not yet

81 quantitatively understood (Sanders, 2007).

82   Another point not sufficiently understood is the uncertainty of predicted velocity. Many have
83   discussed uncertainty in the predicted inundated area, the water stage, the friction factor, and those
84   relationships (e.g, Pappenberger et al., 2005; Horritt, 2006; and Schumann et al., 2007). The
85   inundated area and the inundated water stage are significant indicators for risk estimations; however,
86   uncertainty in velocity has not been addressed well as a result of a lack of an accurate field record
87   indicating flow velocity during inundation. Propagation of the inundated area has been observed as a
88   result of flow motion. Therefore, essentially, the validation of flow motion must be implemented.
89   Unfortunately, it is likely that the inundated area is accurately predicted without an accurate
90   prediction of the dynamic process (flow motion) because the maximum inundated area is almost
91   determined as hydrostatic.
92   In this work, inundation flow on three representative terrain models, with and without artificial
93   elevation error, was evaluated in order to systematically and quantitatively evaluate the effect of
94   elevation uncertainty on the calculated inundation flow. A high-resolution grid (3 m in spacing)
95   calculation was treated as a benchmark following a sensitivity analysis on grid spacing. The
96   accuracy of the predicted result was evaluated based not only on the inundated area and the water
97   depth, but also on the velocity and flow momentum. The predictability of inundation flow over
98   actual topography is also discussed.
99
100   **2. Numerical flow model**
101
102   In this work, two-dimensional (2D) shallow-water equations were solved using a shock-capturing,
103   finite-volume scheme on an unstructured triangulate grid system (Tsubaki et al., 2008; Tsubaki and
104   Fujita, 2010). The following fundamental equations were used:

105
$$\frac{\partial h}{\partial t} + \frac{\partial hu}{\partial x} + \frac{\partial hv}{\partial y} = 0, \tag{1}$$

106
$$\frac{\partial uh}{\partial t} + \frac{\partial u^2 h}{\partial x} + \frac{\partial uvh}{\partial y} + \frac{g}{2}\frac{\partial h^2}{\partial x} - gh\frac{\tau_{sx} - \tau_{bx}}{\rho} = 0, \tag{2}$$

107
$$\frac{\partial vh}{\partial t} + \frac{\partial uvh}{\partial x} + \frac{\partial v^2 h}{\partial y} + \frac{g}{2}\frac{\partial h^2}{\partial y} - gh\frac{\tau_{sy} - \tau_{by}}{\rho} = 0 \tag{3}$$

108   where h is the depth of flow, u and v are the depth-averaged velocity components in the x and y
109   directions, t is the time, and g is the gravitational acceleration. τ_{bx} and τ_{by} are related to the bed slopes
110   in the x and y directions, and τ_{sx} and τ_{sy} are the bottom shear stresses, which are defined as follows:

111
$$\frac{\tau_{bx}}{\rho} = -\frac{\partial z_b}{\partial x}, \frac{\tau_{by}}{\rho} = -\frac{\partial z_b}{\partial y}, \frac{\tau_{sx}}{\rho} = \frac{n^2 u\sqrt{u^2 + v^2}}{h^{4/3}}, \frac{\tau_{sy}}{\rho} = \frac{n^2 v\sqrt{u^2 + v^2}}{h^{4/3}} \tag{4}$$

112   where n is Manning's roughness coefficient and z_b is the local ground elevation.

113   The finite volume method was used to discretize the fundamental equations in the same manner as

114   utilized in Shige-eda et al. (2002) and Shige-eda and Akiyama (2003). The unknown variables were

115   defined at the center of each cell. In order to ensure numerical stability, a flux difference scheme was

116   adopted for the advection and source terms in the basic equations. The permeability of the building

117   was neglected and the slip-wall condition was specified along the boundaries of the buildings. The

118   treatment corresponds to the building-hole (BH) method as defined in Schubert and Sanders (2012).

119   The topography of the domain was accounted for in the calculation as (1) the shape of the wall

120   boundary, (2) the distribution of the cell averaged ground elevation z_b, and (3) the cell representative

121   roughness parameter n. The work presented here focused on the effect of the topographical

122   representation uncertainty, in particular, the error in the distribution of the ground elevation, z_b.

123

124   **3. Topographical data processing**

125   **3.1 The artificial elevation error model**

126   Topographical uncertainties are caused by various factors including systematic and random errors. In

127   this study, based on the fact that the uncertainty of local ground elevation is highly affected by the

128   topography and ground cover (Sithole and Vosselman 2004) as shown in Figure 1, an artificial

129   elevation error, not just random but having spatial structure, was generated using a fractal algorithm

130   (e.g. Bates et al., 1998). The fractal algorithm adopts the midpoint displacement algorithm using a

131   diamond-square algorithm (see Figure 2, Fournier et al., 1982). The basic concept of the algorithm

132   consists of the following: (1) interpolation of the central points in the square grid (Figure 2a and b),

133   and (2) the interpolation of the central points in the diamond grid (Figure 2b and c). A pair of the

134   square grid and the diamond grid interpolations composes one iteration step. The grid point number

135   increases according to interpolation implementations. The interpolation was conducted n_i times to

136   obtain the required grid point number of the topography. At the first few iteration steps, n_f, the

137   interpolation of the elevation was operated as the mean value of four surrounding points. Following

138   iteration steps over n_f steps, additional elevation error was introduced in the interpolated value. The

139   magnitude of the elevation error is adjusted depending on the iteration step, namely the error

140   magnitude B_i is calculated based on the magnitude of the previous step as $B_i = b\,B_{i-1}$, where B_i is the

141   error magnitude at iteration step i, and b (<1) is the reduction rate of the error magnitude per

142   iteration step. The initial grid is a square grid that consists of 2×2 points and the elevation of the

143   four initial points are set as 0 m. In the first n_f steps, the elevation noise is not introduced, so the

144   topography in the first phase is just flat but the grid points are increased exponentially. After n_f steps,

145   elevation error is introduced so that the topography begins to have undulation. The error magnitude

146   is gradually decreased so that larger scaled undulation has a larger magnitude in the elevation, and

147   the smaller scaled undulation has a smaller magnitude in elevation. In this work, the parameters were

148   set as $n_i = 9$, $n_f = 5$, and $b = 0.80$ by considering the balance between the randomness and the

149 regularity of the model error. Here, a generated fractal pattern has grid points of $2^9 \times 2^9$. A factor of

150 1.953 m was set as the grid spacing for the x and y directions, and a domain of 1000 m $\times$ 1000 m for

151 the noise pattern was generated as shown in Figure 3. The generated terrain model shows a structure

152 whose spatial scale ranges from 1.953 m to $1.953\text{m} \times 2^4 = 31.248$ m. Elevation uncertainty in aerial

153 LiDAR measurements depends on device performance and measurement conditions. Bales and

154 Wagner (2009) reported that the uncertainty was less than 30 cm, while Néelz et al. (2006) estimated

155 that the uncertainty in the root mean square was less than 15 cm. Therefore, the typical magnitude of

156 LiDAR elevation error could be 0.15 m; so, in this work, 2σ was specified as 0.15 m. The error

157 distribution $e(x, y)$ is generated based on the random numbers so standard deviation σ_e of distribution

158 $e(x, y)$ can not to be determined in advance to generate error distribution. To adjust the error

159 magnitude as $2\sigma_{e'} = 0.15$ m for the final error pattern $e'(x, y)$, correction

160 $$e'(x, y) = 0.15\,e(x, y)/2\sigma_e \qquad (5)$$

161 was operated. Manning's roughness coefficient n was set to 0.01 in all cases. A larger Manning n is

162 necessary in large grid size calculations and the sensitivity of the roughness coefficient to the

163 calculated results is reduced in high-resolution calculations. The latter comes from the fact that

164 detailed topographical features and small-scale flow structures are directly resolved in the flow

165 simulation within fine grid systems (Casas et al. 2010). The roughness coefficient was treated to a

166 constant and elevation uncertainty. The uncertainty of the roughness parameter and its effects on the

167 calculated results are not discussed in this work.

168

169 **3.2 The three terrain models**

170 Three terrain models were used to explore the relationship among topographical types, inundation

171 flow characteristics, and inundation prediction uncertainty. The first terrain model contained a series

172 of flat terrains with a specific general ground slope. The model elevation uncertainty was overlain

173 onto the base topography (see Figure 4). In this work, this topography set is called Plain topography.

174 The second model set, shown in Figure 5, contained a series of topographies representing rice fields,

175 a typical rural topography in Japan. This topography type was based on the DEM (digital elevation

176 model) with a spatial resolution of 2 m, measured by an aerial LiDAR survey. In this work, this

177 topography is called Rural topography. Each rice paddy parcel was separated by ribbing, forming a

178 rectangular grid in the horizontal plane. As shown in Figure 6, the third model contained an urban

179 topography that included a complex street network and buildings, and is referred to as Urban

180 topography. The ground elevation of Urban topography was set as flat, with a specific ground slope

181 as for Plain topography. The topology of the street and building arrangement was based on 1 m

182 resolution LiDAR data. The vector data of each building shape was extracted from the DSM (digital

183 surface model) and the DEM (Tsubaki and Fujita, 2010). The extracted vector data set was used as

184 the shape of the slip wall boundary in the unstructured grid. However, the detail of the elevation

185 distribution in actual urban areas is omitted in this work so that we could concentrate on the effect of

186 elevation uncertainty on the calculated results. The effects of this simplification were evaluated, in

187 detail, by Mignot et al., 2006. As measured by aerial LiDAR measurements, topography patterns

188 used in the second and third models were based on actual topography. Additional ground slope and

189 elevation uncertainties were overlain onto the elevation distribution. Flows calculated with a series

190 of topographies were compared with one another in order to evaluate the sensitivity of the general

191 ground slope and the elevation uncertainty on the predicted flow. The three topography sets were

192 discretized in the triangulate grid, where each grid size was 3, 5, 10, and 20 m. Variation in the grid

193 size was utilized to evaluate the sensitivity of the grid size on the calculated flow. The fundamental

194 effects of grid size on calculated results have been reported previously by, for example, Horritt and

195 Bates, 2001; Horritt et al., 2006; and Tsubaki et al., 2007. For specifying the grid size discussed in

196 the following text, the values "03 m", "05 m", "10 m", and "20 m" are used in the figures and the

197 text. The three error patterns are specified as "ErrorA", "ErrorB", and "ErrorC". The algorithm used

198 to generate three error patterns was identical and overall the error magnitude, $\sigma_{e'}$, was also identical

199 but a different table of random numbers was employed.   Therefore, the spatial distribution of the

200 pattern differed completely for evaluating the universal effect of elevation error, not only error

201 pattern dependent features. Obviously, the actual spatial pattern of the topographical error is

202 impossible to identify in practice. Thus, unique effects due to specific error patterns are separated in

203 this work using three different error patterns, and the typical universal effects caused by elevation

204 error are discussed.

205 For the inflow boundary of each topography case, a steady flow rate, Q, of 50 m³/s (Plain), 30 m³/s

206 (Rural), and 25 m³/s (Urban) was configured. The lengths of the inflow boundaries were 20 m

207 (Plain), 20 m (Rural), and 25 m (Urban). Inflow conditions modeled sudden inundation due to rapid

208 embankment breaching.

209

210 **4. Result**

211 In this section, the grid size effect in the expansion of an inundated area was investigated in order to

212 validate the flow model. Then, the effects of elevation error and grid size on the Plain, Rural, and

213 Urban topographies are discussed. Finally, the effects of topographical uncertainty on calculated

214 local flow parameters are explored.

215

216 **4.1 Grid size effects**

217 In this subsection, the grid size effect on the propagation of inundation water is explored for

218 validating the flow model that included both the discretized fundamental equations and the

219 calculation grid (Bales and Wagner 2009). The topographical data discussed in this subsection

220   retained no elevation error.

221

222   **4.1.1 Plain topography**

223   In Figure 7, hydrographs of water volume in the calculation domain, using different grid sizes, are

224   depicted. As shown in the figure, the inundation water volume was not sensitive to grid size and was

225   consistent with the exact value (i.e. $V = Qt$, where V is the water volume (m^3), Q (= 20 m^3/s) is the

226   inflow discharge, and t is the elapsed time (s) after inundation begins. The results indicate that the

227   numerical model, including the treatment of the wet-dry boundary, was perfectly conservative, at

228   least in mass.

229   Time-series changes of the inundated area in the various grid sizes and for the two bed slopes are

230   compared in Figure 8. As shown in Figure 8a, for the case of a medium slope, a low sensitivity for

231   the grid size to the expansion of an inundated area was observed (a 5% difference between the 03 m

232   and 20 m grids). The results of the 03 m and 05 m grids were approximately identical (a 0.5%

233   difference in the inundated area). The results of the milder slope cases ($I = 1/1000$ and $I = 1/2000$)

234   are not provided here, however, the profile was quite similar to Figure 8a. In the case of a steep slope

235   ($I = 1/50$, as shown in Figure 8b), the hydrograph of the inundated area differed along with the grid

236   size. The graph indicates that the result, calculated using a smaller grid size, displayed a smaller

237   inundation area. In order to investigate the cause of inadequate behaviour, as observed for the steep

238   slope case, snap-shots of inundated water depth for the small and large grid cases at the same instant

239   ($t = 200$ s) are presented in Figure 9. The result of the small grid (in the upper half of Figure 9) is

240   longer and thinner in the downslope direction in the shape of the inundated area, as compared to

241   those of the coarse grid result depicted in the lower half of Figure 9. For the steep slope condition,

242   flow was determined at the upstream side because the flow was super-critical, and the propagation

243   pattern of inundation flow is sensitive to the local flow surrounding the inflow boundary. As

244   indicated in Figure 9, the angle of expansion of the flow surrounding the inflow point in the coarse

245   grid result was larger than that of the fine grid case. In cases of milder slope, the propagation pattern

246   is mainly governed by a water surface slope surrounding the propagating edge and is insensitive to

247   local flow at the inflow point. The difference in the mechanism of expansion of inundation water,

248   depending on the general ground slope, caused a difference in the sensitivity of the grid size to the

249   propagation of inundation.

250   In conclusion, in this subsection, a grid size smaller than 10 m was sufficient for representing the

251   rapid expansion of inundation water for Plain topography with a 20 m width inflow boundary. On

252   the other hand, a grid size finer than 10 m was needed in order to resolve the sudden change of flow,

253   in case local transient flow has a major impact on the expansion of the inundated area.

254

255   **4.1.2 Rural topography**

256

257   In Figure 10, two time-series for the inundated area, calculated using fine (03 m) and medium (05 m)
258   grids, are compared. The general trends for the inundated area expansion are identical to one another,
259   but the result calculated using the 05 m grid was overestimated by a few percent, as compared with
260   the result of 03 m. The overestimation trend in the larger grid result was similar to the result
261   observed for Plain topography with a steep slope (see Figure 8b). In Figure 11, the instantaneous
262   distributions of water depth, as calculated using the 03 m and 05 m grids at $t = 1000$ s, are depicted.
263   The general pattern for water depth was quite analogous but a difference was observed surrounding
264   the wet-dry boundary. In this area, due to a small water depth, the flow was quite sensitive to the
265   small difference in ground elevation and led to the difference in the time series change in the
266   inundated area. In Figure 12, histograms of water depth at $t = 1000$ s for the 03 m and 05 m cases are
267   provided. Differences were observed in the shallow region ($h < 0.1$m). However, the profiles, with
268   the exception of the shallow region, were almost similar.
269   In summary, for Rural topography, a difference between the 03 m and 05 m results was observed in
270   the area surrounding the outline of the inundated area. However, the general propagation pattern of
271   inundation was insensitive to grid size in the range below 5 m. Rural topography was represented by
272   the distinguishing ground undulation pattern, which has a spatial scale over a few meters and
273   regulates the inundation expansion pattern. Thus, the pattern of the calculated inundation expansion
274   was almost insensitive to the grid size if the discretised grid represented the distinguishing ground
275   pattern.

276

277   **4.1.3 Urban topography**

278

279   Urban topography was represented by building arrangement and sloped ground. In Figure 13, the
280   time-series of the inundated area for the steep sloped case ($I = 1/50$) and the mild sloped case ($I =$
281   1/1000) are depicted. For both steep and mild slope cases, the time-series change of the inundated
282   area was insensitive to grid size. In Figure 14, the distributions of water depth at t = 400 s, as
283   calculated by the 03 m and 05 m grids, are compared. The distributions of the two grid sizes are
284   generally identical. The result supports the idea that the calculated results of urban topography are
285   insensitive to grid size because the unstructured grid is capable of representing the irregular shape of
286   a complex building boundary and because the representation of the building boundary is less subject
287   to the difference in grid size, since an unstructured grid system is used.

288

289   **4.2 The impact of elevation error in Plain topography**
290   In Figure 15, water depth distributions of inundation flows on different ground slopes, with and
291   without artificial elevation errors, are depicted. Even if the error is added, the topography in this

292　section is almost flat. Therefore, the inundated area expands rapidly with shallow water depth. In

293　cases where steep slopes exist (the upper contours of Figure 15), the inundated water flows in the

294　down-slope direction (the right side) rapidly, and the inundated area reaches 2,000 m from the

295　inflow point in the down-slope direction at $t = 300$ s.

296　In cases of a mild slope condition (the bottom contours in Figure 15), the inundated areas expand

297　concentrically near the inflow area and the inundated water depth is, in general, quite shallow (h <

298　0.1 m for most areas). The magnitude of the elevation error in the ErrorA case is 0.15 m, so the

299　magnitude of the water depth is equal in magnitude to the elevation error (Pasternack et al., 2006),

300　and the water flowing on the Plain topography with the elevation error suffers a major impact due to

301　elevation error. For the steep slope case, the relative impact due to elevation error impact is limited

302　as compared with those of milder slope cases.

303　Figure 16 compares the time-series changes of the inundated area calculated using a 03 m grid but a

304　different bed slope and error patterns. The results of the steep slope ($I = 1/50$) with and without

305　model error were almost identical. The results of the milder slope cases ($I = 1/300$ and $I = 1/1000$)

306　indicated a larger impact on inundation propagation due to elevation error. The effect of error

307　addition emerged as an underestimation of the inundated area. A small undulation disturbed the

308　inundation flow propagation. In addition, dents formed by elevation error impounded the water

309　volume, which spread faster in cases of an original flat topography. In Figure 17, the distributions of

310　the Froude number in cases of $I = 1/300$ and $I = 1/1000$, at $t = 300$ s, are compared. The inundation

311　flow in a case of $I = 1/300$ without error (the upper-left figure in Figure 17) was super-critical in

312　almost all areas. The area close to the inflow point was also super-critical for the $I = 1/1000$ case (the

313　lower-left figure in Figure 17), but the expanding front was sub-critical in this case. The results

314　calculated using elevation error showed a completely different distribution. The Froude number is

315　one of the key factors in water propagation for the shallow water condition. In the case of inundated

316　water spreading broadly in the horizontal and thinly in depth, the flow is quite sensitive to the small

317　undulation of ground elevation. As shown in Figure 17, inundation flow structure is drastically

318　changed due to elevation error. The topography data obtained using LiDAR contains elevation error,

319　and this error causes (i) an underestimation of the expansion of the inundated area, and (ii) a change

320　in the flow direction of inundation. The undulation, whose spatial scale is smaller than the grid size,

321　is filtered out during grid generation; however, the undulation, whose spatial scale is larger than the

322　grid size, is represented by the calculation grid. Undulation is due both to the originated topography

323　and the measurement error. The effect of small scale topographical features on the flow is modelled

324　in the roughness parameter within the numerical model. Small scale undulation, due to the error,

325　causes a limited effect on the flow because small undulation is filtered out during the gridding

326　process. Large scale elevation uncertainty, caused by structural or systematic error (e.g. the effect of

327　vegetation cover) leads to a considerable difference in the propagation pattern of inundation.

328

4.3 The effect of grid size and elevation uncertainty on Rural topography

In Figure 18, inundated flow structures calculated using different grid size and error patterns are compared. The structure of the flow is depicted using the Line Integral Convolution (LIC) method (Cabral and Leedom, 1993). LIC is a texture based flow visualization method. The direction of the texture in Figure 18 corresponds to the local flow direction. The contrast of the texture correlates with the flow rate per unit width, hU. The results obtained from the four cases, in general, show a similar structure. Inundated water overflows on the ribbing, and a critical flow and the control section are formed above the ribbing. The similar flow structure is represented regardless of the noise addition. However, as shown in Figure 18, the location where inundated water overflows to a neighboring paddy parcel differs depending upon the difference of grids.

The pattern of the flow route and the circulation observed within each rice field cell is quite complex and differs when the grid size and the elevation error pattern are changed, indicating that the flow structure within the rice field cell is quite sensitive to topographical uncertainty and is difficult to correctly predict. Although flow structure within the rice field cell affects damage to the planted crop, the global inundation propagation is less subjected to flow circulation within the rice-paddy cell, so the general pattern of expansion of the inundation is identical regardless of grid size and error pattern changes, as confirmed in Figure 18.

Figure 19 compares the time series change of the inundation area calculated using a 03 m grid and different elevation error patterns. The figure shows that the addition of elevation error causes a slight underestimation in the expansion of the inundation area. A minor difference was observed in the distribution of the inundated area (as shown in Figure 18). The underestimation trend in the inundated area following error appending was also observed for Plain topography (Figure 16). An underestimation in Rural topography was caused by flow disturbance and water storage effects (the effect of the latter was discussed in Horritt and Bates, 2001).

In conclusion, the general structure of inundation flow regulated by the structure of topography in a rural area, as shown in Figure 18, consisting of rice paddy cells and ribbings, is represented using detailed topographical data. However, the circulation of flow within each rice paddy, as well as the exact location of overflows that arise on ribbings, are quite sensitive to small differences in the topographical representation. In this sense, local flow parameters, especially the local velocity and the momentum of inundation flow within complex topographies are quite difficult to estimate. As a result, one must pay attention to difficulties in the prediction of local flow when implementing risk estimations based on local flow parameters, e.g. the assessment of risk that is related to the flow intensity (e.g. Koshimura et al. 2009), the estimation of sediment transport in the flood plain, etc.

4.4 The effect of grid size and elevation uncertainty on Urban topography

364

365 Urban topography consists of a complex impermeable boundary wall that represents buildings
366 concentrated in a dense state. The ground is flat but has a constant bed slope (see Table 1). As
367 described in Section 3.1, cases with error contain a small undulation in the elevation distribution.
368 Figure 21 shows the time series of the inundated area calculated using grids with and without
369 elevation error. The steep sloped result (Figure 21a) shows the very slight effect of elevation error on
370 inundated area expansion. The medium slope result (Figure 21b) shows a greater influence for
371 elevation error in the expansion of the inundation area as compared to the results from steep slope
372 cases. The elevation error causes an approximate 25% underestimation in the growth of the
373 inundation area in the medium slope case. The trend has already been observed for Plain topography
374 (as discussed in Figure 16), and Rural topography (depicted in Figure 19). Results for the $I = 1/1000$
375 case of Urban topography are not depicted in Figure 21. However, the trend is similar to the result of
376 the $I = 1/300$ case. Namely, a certain level of under-estimation (35%) of inundation area expansion
377 was observed for a condition of $I = 1/300$ with elevation errors. As discussed in Section 4.2, the
378 underestimation is due to the impact of both flow disturbance and water storage by the undulation
379 formed due to elevation error.

380

381 In Figure 22, the flow structures of the urban floodplain, calculated using six different calculation
382 grids, are depicted using the LIC method. The major water volume of inundated flow propagates
383 throughout a broad street (depicted as a high contrast hair-line pattern in the street shown in Figure
384 22). Not only the broad street, but small streets connected to the broad street also contributed to
385 spreading the inundated water, and a complex flow network bounded by urban topography emerged.
386 As depicted in Figure 22, the structure of the flow is basically identical for the six cases. Differences
387 in the ground slope impacted the degree of lateral dispersion of inundation flow, but the sensitivity
388 of the ground slope changed and the difference in the propagation pattern was limited as compared
389 with the result for Plain topography (see Figure 15). The inundation flow expansion was affected by
390 grid size and elevation error in a similar manner as observed for the Plain and Rural cases, but
391 sensitivity to grid size and elevation error was limited as compared to the Urban case.
392 In Figure 23, close-up images of the flow structure surrounding the inflow area are compared.
393 Observed again is that the general flow structure is not sensitive to grid size and elevation error.
394 However, the detail for the flow network in the small street system was impacted by differences of
395 grid size and elevation.

396

397 **4.5** *The flow prediction uncertainty*
398 In this section, the uncertainty of flow information, estimated using the flow simulation by
399 considering the topographical uncertainty, is quantitatively discussed. In order to compare

400 instantaneous and local flow conditions between calculated results with different grid sizes, the flow

401 parameters were interpolated on the grid at a 20 m interval in the x and y directions. In order to

402 obtain the flow data at each grid point, cells whose centers were located within 5 m of the grid point

403 were selected. Then, the mean of the flow parameters of the selected cell center values were

404 calculated. For cases in which all cells close to the grid point were dry or quite shallow in water

405 depth ($h < 0.05$m), the flow information at this grid point was not used in the following statistical

406 calculation. The differences of the flow parameters (water depth, h; water level, H; flow rate per unit

407 width, hU; and the momentum flux per unit width, hUU) between the two calculation cases for the

408 entire corresponding grid points were calculated; then, the standard deviation of the difference in the

409 flow parameters were calculated. Here, U is the magnitude of the local velocity ($U = \sqrt{u^2 + v^2}$). The

410 standard deviation of the elevation, σ_z, was also calculated. The parameter σ_z indicates the magnitude

411 of the elevation error ($2\sigma = 0.15$ m), but is not completely identical to the magnitude of the model

412 elevation error since σ_z is impacted by the grid size and the spatial filtering effect due to gridding.

413 The results are listed in Tables 2, 3, and 4 for the Plain, Rural, and Urban cases, respectively.

414 For a case of Plain topography (Table 2), the elevation of NoError cases has no undulation and is

415 completely plain. Therefore, the standard deviation of the 05m-NoError and 10m-NoError cases

416 indicates that the error due to discretization and the magnitude of the standard deviations are

417 sufficiently small. The deviations in water depth and water level are comparable to one another and

418 are increasingly proportional to the increment of the grid size. As shown in Figure 15, the water

419 depth range spanned 0.0 to 0.3 m, and the standard deviations for water depth, σ_h, and water level,

420 σ_H, were small relative to the water depth magnitude. With the exception of the area close to the

421 inflow boundary, the flow rate per unit width, hU, was found to be in the range from 0.0 to 0.3 m^2/s.

422 The relative magnitude of σ_{hU} in NoError cases was sufficiently small. The standard deviation of the

423 momentum flux per unit width, σ_{hUU}, was one order larger than those of σ_{hU} for the 05m-NoError

424 and 10m-NoError cases. The results shown in Table 2 imply that the flow parameters were quite

425 sensitive to elevation uncertainty and that local flow parameters related to flow motion were almost

426 unreliable under the presence of the elevation uncertainty.

427 The result of the Rural case, as indicated in Table 3, showed similar trends as for the Plain case.

428 However, the σ_{hU} and σ_{hUU} for 05m-NoError in the Rural case were comparably larger than those for

429 the 05m-NoError in the Plain case. Inundated water overflowed at the ribbing and was locally

430 accelerated around the critical-section at the overflow point. The flow condition of the overflow was

431 determined by the local topography surrounding the ribbing. Therefore, the small difference of the

432 ribbing representation made a large difference on the overflow condition. Circulation in the rice field

433 cell following overflow at the ribbing was quite sensitive to the overflow condition and led to a

434 larger σ_{hU} and σ_{hUU}. Inundated water is stored in the rice field cell before overflow to the next paddy

435 begins, such that the range of water depth in rural cases reaches 0.5 m. The relative magnitude of the
436 standard deviation of the water depth is small. In this context, if the ground elevation distribution has
437 a distinct structure, such as rice field cells separated by ribbing in the Rural topography, the
438 inundated water will be stored in the areas surrounded by the ribbing (structured dents). The
439 location, area, and water storage capacity of the structured dents are almost conserved under the
440 influence of small elevation uncertainty. Therefore, the water level of the inundation water stored in
441 the structured dents is also not very sensitive to small grid errors. On the other hand, the unit width
442 discharge and momentum flux are sensitive to elevation uncertainty because the flow is accelerated
443 mainly at the boundary between consecutive structured dents (see Figure 20). The flow acceleration
444 is regulated by local ground elevation surrounding the ribbing. Thus, small elevation error at the
445 overflow points causes major changes in the direction and magnitude of local inundation flow.

446 The error magnitude of the calculated water depth, due to elevation error, can be estimated as
447 proportional to the magnitude of the elevation uncertainty. The error in water stage (σ_H) is
448 comparable to water depth uncertainty (σ_h), and, thus, the uncertainty in elevation (σ_z). Obviously,
449 there are close relationships among water stages, water depth, and elevation, namely, $H = z + h$.
450 Similar magnitudes for σ_h, σ_H, and σ_z imply that there are correlations amongst h', H', and z'.

451 To confirm the flow structure and its relationship to prediction error, the relationship between flow
452 parameters at $t = 1000$ s and a distance from the inflow point l are depicted in Figure 24. In Figure
453 24a, the water stage profile of the 03m-No error case is plotted. A systematic trend can be observed
454 in the profile of the water stage. Each cluster of the plot corresponds to the water stored in each
455 paddy cell. Figure 24b shows the distribution of the root mean square (RMS) of the water stage
456 errors, defined as follows:

$$457 \qquad H'_{\text{RMS}} = \frac{1}{3} \sum_{j=A,B,C} \sqrt{\frac{1}{N_{(j)}} \sum_{i}^{N(j)} \left(H_{\text{Err}(j)} - H_{\text{NoErr}}\right)^2} \; . \qquad (6)$$

458 H'_{RMS} is the average error of the three elevation errors. The H'_{RMS} plot shows a weak relationship for
459 the systematic bias observed in Figure 24a, and the water stage error is kept at a constant level using
460 increments of distance from the inflow. The unit width discharge distribution is shown in Figure 24c.
461 In the area close to inflow ($l < 200$ m), a large unit width discharge shatter was observed and
462 corresponds to jet flow surrounding the inflow point. The plot of the RMS error of the unit width
463 discharge (Figure 24d) shows a similar profile and magnitude for the original unit width discharge
464 plot (Figure 24c). In the area far from inflow ($l > 300$ m), the RMS error of unit width discharge
465 keeps an almost constant level such as the error of the water stage. One should note that in the area
466 away from the flow inflow point ($l > 300$ m), the order of the original unit width discharge, hU, and
467 the magnitude of the error, hU'_{RMS}, are almost identical - indicating that local flow is quite uncertain
468 in cases where the elevation contains uncertainty.

469 The standard deviations of hU for Urban topography (as shown in Table 4) are small as compared to
470 the Rural case. In the case of Urban topography, the arrangement of the buildings and road networks
471 were kept almost constant among the different grid sizes and elevation error patterns. Inundation
472 flow was regulated by the arrangement and the buildings, and the elevation distribution and
473 horizontal topographical features had a smaller impact on the inundation. Therefore, there was a
474 relatively smaller error for the unit width flow rate and momentum flux predictions for the Urban
475 case. However, the magnitudes of the unit width flow rate and the momentum flux were around hU
476 $= 0.3$ m^2/s and $hUU = 0.3$ m^3/s^2. Therefore, the standard deviations of hU and hUU in cases that
477 contained elevation errors were relatively large ($\frac{\sigma_{hU}}{hU} \approx 0.2, \frac{\sigma_{hUU}}{hUU} \approx 0.4$). Standard deviations for
478 water depth were comparable to elevation uncertainty in cases with elevation errors. A similar trend
479 was observed for the Plain and Rural cases.
480 In order to investigate the spatial bias of the flow and the prediction uncertainty in the Urban case,
481 the relationship between distance from the inflow and the flow parameters are depicted in Figure 25.
482 The structure of the water stage profile shown in Figure 25a illustrates that a continuous but
483 fluctuating downward trended water profile was observed along the street network. The water-stage
484 error shown in Figure 25b shows a slight increasing trend with the increment of distance. In Figure
485 25c, the profile of the unit width discharge indicates that certain measurements of inundated water
486 have a small unit width discharge, but that a larger unit width discharge is concentrated on the
487 specific street. As depicted in the bright texture in Figure 23, the profile also indicates that most of
488 the water mass is transferred to the specific flow network. The unit width discharge error shown in
489 Figure 25d shows a similar pattern to the distribution shown in Figure 25c. The unit width discharge
490 error at the propagating edge ($l > 400$ m) is raised and indicates that local flow at the propagating
491 front has a comparatively large uncertainty.
492 Differences in topographical structure have a great impact on inundation flow propagation and the
493 characteristics of prediction uncertainty, as shown in the differences in the profiles between Figure
494 24 and Figure 25, indicating that inundation flow has a structure and that inundation flow structure
495 has a close relationship to topographical structure. A further important point is that the magnitude of
496 the prediction uncertainty is also strongly regulated by topographical structure.
497
498 **5. Conclusion**
499 In this work, the effect of elevation uncertainty on predicted inundation flow was evaluated. Three
500 representative topographies were designed. The sensitivities of grid size and elevation error to the
501 calculated flow were investigated from the view point of the inundated area increment, the water
502 depth distribution, the flow structure, and the quantitative evaluation of local flow parameters. The
503 results suggest the following:

504   (1) The result calculated by the larger grid size displayed a shallower and faster water propagation of
505   inundation as compared to the result calculated using a finer grid with the same roughness
506   parameter, because rapidly-varied 2D flow is inadequately resolved using a coarse grid calculation.
507   The smoothing effect of the elevation distribution also caused shallow and rapid inundation
508   propagation in cases where a coarse grid size was utilized. Calibration of the roughness parameter is
509   essential for adjusting the effect of grid size on the inundation propagation in cases where a large
510   grid size is utilized.
511   (2) When the elevation distribution has a large scale structure (e.g. the structured dents in Rural
512   topography, and the street network in Urban topography), inundation flow is regulated by the
513   structure of the topography. The large-scale topographical structure is well kept within spatial
514   features and is insensitive under the influence of elevation uncertainty. Therefore, water depth and
515   water level can be predicted using a comparatively high accuracy in cases of inundation on
516   structured topography, as compared with flow estimations in Plain topography. Since the
517   acceleration of flow occurs in specific areas and since small differences in topography in specific
518   areas cause a major change in inundation flow structure, local flow and flow related parameters
519   suffer a great impact due to elevation error.
520   (3) The predicted local water depth, h, contains an uncertainty whose magnitude is almost identical
521   to the magnitude of the elevation uncertainty. The standard deviation of hU is impacted both by
522   elevation error and topographical structures. The magnitude of the standard deviation of hU is
523   comparable to the magnitude of hU in cases where the topography has an elevation uncertainty. The
524   σ_{hUU} is almost two-times larger than σ_{hU} in cases where the elevation has uncertainty. The relative
525   error of the momentum flux is large as compared to that in the unit width discharge.
526
527   The work presented here implies that some part of the calculated flow parameters contain significant
528   uncertainty. Therefore, the results obtained from this work should be kept in mind when flow
529   parameters calculated using a detailed inundation simulation are used for risk estimations related to
530   the flow velocity (e.g. the difficulty evacuation (Koshimura et al., 2006) or the risk failure for
531   structures (Koshimura et al., 2009)). On the contrary, the reason inundated water was mainly utilized
532   in the risk estimation may be related to the poor accuracy of the magnitude of predicted inundation
533   flow. Research on inundation flow structure (Tsubaki et al., 2007) may be useful for determining key
534   factors of topography that determine inundation expansion. By considering the dominant factor of
535   topography, it may be possible to improve both the calculation efficiency and the accuracy, not only
536   for detailed inundation flow type simulations but also for integrated type simulations in inundation
537   prediction methods (e.g. Yu and Lane, 2005). The effect of topographical uncertainty in adverse
538   sloped ground is not discussed in this paper but important area to be analysed to advance our
539   knowledge of structural damage risk estimation in tsunami disaster.

540 Discussion in this work is limited to a comparison of the calculated results. A comparison with the
541 field record or experimental data is not included mainly because the discussion presented in this
542 work is quite sensitive to boundary condition uncertainty, and because it is quite difficult to
543 determine sufficient accuracy and resolution for boundary conditions of actual inundation cases or
544 physical models for complex topography inundation. The inadequacy of the calculation model itself
545 is also outside the scope of this work. Here, the discussion has limitations for some of the conditions
546 described above. However, the findings obtained in this study contribute to our understanding of the
547 characteristics of the uncertainty involved in the predicted flow parameters under the effect of
548 topographical data uncertainty. The predictability of local flow parameters on inundation flow within
549 complex topography has not, thus far, been seriously addressed. The results obtained from this study
550 indicate that more careful considerations should be made regarding the uncertainty of calculated
551 results since calculated flow parameters, especially those related to water velocity, contain large
552 uncertainty.
553 Elevation accuracy can be improved in regards to instrument improvement, operational control (e.g.
554 lower and slower flight in aerial LiDAR measurements), and refined post-process of the measured
555 data. Such improvements may, in some respects, reduce the error of the calculated result. On the
556 other hand, physical uncertainty, for example, terrain alternation after the topography survey such as
557 for vegetation growth or decay and for changes in the arrangements of parked cars and temporal
558 structures, still remains after the improvement of accuracy in topography measurements. Again, we
559 must acknowledge that calculated flow dynamics contain considerable uncertainty for cases where
560 the predicted flow dynamics are utilized to predict risks related to water flow.
561
562

563 **REFERENCES**
564 Abdullah, A.F., Vojinovic, Z. and Price, R.K., 2011, Improved Methodology for Processing Raw
565   LIDAR Data to Support Urban Flood Modelling - Accounting for Elevated Roads and Bridges,
566   *Journal of Hydroinformatics*, doi:10.2166/hydro.2011.009.
567 Alcrude, F and Garcia-Navarro, P., 1993, A high-resolution Godunov-type scheme in finite volumes
568   for the 2D shallow-water equations, *International Journal for Numerical Methods in Fluids*, 16,
569   489-505.
570 Anastasiou, K. and Chan, C.T., 1997, Solution of the 2D shallow water equations using the finite
571   volume method on unstructured triangular meshes, *International Journal for Numerical Methods
572   in Fluids*, 24, 1225-1245.
573 Bales, J.D. and Wagner, C.R. 2009, Sources of uncertainty in flood inundation maps, Journal of
574   *Flood Risk Management*, 2, 139-147.

575 Bates, P.D., Horritt, M. and Hervouet, J.M., 1998, Investigating two-dimensional, finite element
576   predictions of floodplain inundation using fractal generated topography, *Hydrological Processes*,
577   12, 1257-1277.

578 Bates, P.D., 2003, Remote sensing and flood inundation modeling. *Hydrological Processes*, 18(13):
579   2593-2597.

580 Cabral, B. and Leedom, L., 1993: Imaging vector fields using line integral convolution, *Proc. 20th*
581   *annual conf. on Computer graphics and interactive techniques SIGGRAPH 93*.

582 Caleffi, V., Valiani, A. and Zanni, A., 2003, Finite volume method for simulating extreme flood
583   events in natural channels, *Journal of Hydraulic Research*, 41(2), 167-177.

584 Casas, A., Lane, S.N., Yu, D. and Benito, G., 2010, A method for parameterizing roughness and
585   topographic sub-grid scale effects in hydraulic modeling from LiDAR data, *Hydrology and Earth*
586   *System Science*, 14, 1567-1579.

587 Chuntian, C., Chunping, O. and Chau, K.W., 2002, Combining a fuzzy optimal model with a genetic
588   algorithm to solve multiobjective rainfall-runoff model calibration, *Journal of Hydrology*,
589   268(1-4), 72-86.

590 Cobby, D.M., Mason, D.C., Horritt, M.S. and Bates, P.D., 2003, Two-dimensional hydraulic flood
591   modelling using a finite-element mesh decomposed according to vegetation and topographic
592   features derived from airborne scanning laser altimetry, *Hydrological Processes*, 17, 1979-2000.

593 Fournier, A, Fussel, D, and Carpenter, L., 1982, Computer Rendering of Stochastic Models.
594   *Communications of the ACM*, 25: 371-384.

595 Horritt, M.S. and Bates, P.D., 2001, Effects of mesh resolution on a raster based model of flood
596   flow, *Journal of Hydrology*, 253, 239-249.

597 Horritt, M.S., Bates, P.D. and Mattinson, M.J., 2006, Effects of mesh resolution and topographic
598   representation in 2D finite volume models of shallow water fluvial flow, *Journal of Hydrology*,
599   329, 206-314.

600 Horritt, M.S., 2006, A methodology for the validation of uncertain flood inundation models, *Journal*
601   *of Hydrology*, 326, 153-165.

602 Koivumäki, L., Alho, P., Lotsari, E., Käyhkö, J., Saari, A. and Hyyppä, H., 2010, Uncertainties in
603   flood risk mapping: a case study on estimating building damages for a river flood in Finland,
604   *Journal of Flood Risk Management*, 3, 166-183.

605 Koshimura, S., Katada, T., Mofjeld, H.O. and Kawata, Y. 2006, A method for estimating casualities
606   due to the tsunami inundation flow, *Natural Hazards*, 39, 265-274.

607 Koshimura, S., Oie, T., Yanagisawa, H. and Imamura, F., 2009, Developing fragility functions for
608   tsunami damage estimation using numerical model and post-tsunami data from Banda Aceh,
609   Indonesia, *Coastal Engineering Journal*, 51(3), 243-273.

610   Mason, D.C., Horritt, M.S., Hunter, N.M. and Bates, P.D., 2007, Use of fused airborne scanning
611   laser altimetry and digital map data for urban flood modeling, *Hydrological Processes*, 21,
612   1436-1447.
613   McKean, J., Nagel, D., Tonina, D., Bailey, P., Wright, C.W., Bohn, C. and Nayegandhi, A. 2009,
614   Remote se sing of channels and riparian zones with a narrow-beam aquatic-terrestrial LiDAR,
615   Remote Sensing, 1, 1065-1096, doi:10.3390/rs1041065.
616   Mignot, E., Paquier, A. and Haider, S., 2006, Modeling floods in a dense urban area using 2D
617   shallow water equations, *Journal of Hydrology*, 327, 186-199.
618   Neal. J.C., Bates, P.B., Fewtrell, T.J., Hunter, N.M., Wilson, M.D. and Horritt, M.S., 2009,
619   Distributed whole city water level measurements from Carlisle 2005 urban flood event and
620   comparison with hydraulic model simulations, *Journal of Hydrology*, 368, 42-55.
621   Neal, J.C, Fewtrell, T.J, Bates, P.B. and Wright, N.G. 2010, A comparison of three parallelization
622   methods for 2D flood inundation models, *Environmental Modelling & Software*, 25: 398-411.
623   Néelz, S., Pender, G., Villanueva, I., Wilson, M., Wright, N.G., Bates, P., Mason, D. and Whitlow,
624   C., 2006, Using remotely sensed data to support flood modelling, *Water Management*, 159, Paper
625   14106.
626   Pasternack, G.B., Gilbert, A.T., Wheaton, J.M. and Buckland, E.M. 2006, Error propagation for
627   velocity and shear stress prediction using 2D models for environmental management, *Journal of
628   Hydrology*, 328, 227-241.
629   Pappenberger, F., Beven, K.J., Horritt. M. and Blazkova, S. 2005, Uncertainty in the calibration of
630   effective roughness parameters in HEC-RAS using inundation and downstream level
631   observations, *Journal of Hydrology*, 302, 46-69.
632   Pappenberger, F., Beven, K.J., Ratto, M. and Matgen, P. 2009, Multi-method global sensitivity
633   analysis of flood inundation models, *Advances in Water Resources*, 31, 1-14.
634   Sanders, B.F, 2007, Evaluation of on-line DEMs for flood inundation modeling, *Advances in Water
635   Resources*, 30, 1831-1843.
636   Sanders, B.F., Schubert, J.E. and Detwiler, R.L. 2010, ParBreZo: A parallel, unstructured grid,
637   Godunov-type, shallow-water code for high-resolution flood inundation modeling at the regional
638   scale, *Advances in Water Resources*, 33, 1456-1467.
639   Schubert, J., Sanders, B.F., Smith, M.J and Wright, N.G., 2008, Unstructured mesh generation and
640   landcover-based resistance for hydrodynamic modeling of urban flooding, *Advances in Water
641   Resources*, 31, 1603-1621.
642   Schubert, J. and Sanders, B.F., 2012, Building treatments for urban flood inundation models and
643   implications for predictive skill and modeling efficiency, *Advances in Water Resources*, 41,
644   49-64.

645 Schumann, G., Matgen, P., Hoffmann, L., Hostache, R., Pappenberger, F. and Pfister, L. 2007,
646   Deriving distributed roughness values from satellite radar data for flood inundation modelling,
647   *Journal of Hydrology*, 344, 96-111.

648 Schumann, G., Cutler, M., Black, A., Matgen, P., Pfister, L., Hoffmann, L. and Pappenberger, F.,
649   2008, Evaluating uncertain flood inundation predictions with uncertain remotely sensed water
650   stages, *International Journal of River Basin Management*, 6(3), 187-199.

651 Shamseldin, A.Y., 1997, Application of a neural network technique to rainfall-runoff modeling,
652   *Journal of Hydrology*, 199(3-4), 272-294.

653 Shigeda, M, Akiyama, J, Ura, M, Jha, AK, and Arita, Y., 2002, Numerical simulations of flood
654   propagation in a flood plain with structures, *Journal of Hydroscience and Hydraulic Engineering*
655   20(2): 117–129.

656 Shige-eda, M. and Akiyama, J. 2003, Numerical and experimental study on 2D flood flows with and
657   without structures, *Journal of Hydraulic Engineering*, 129(10), 817–821.

658 Sithole, G. and Vosselman, G. 2004, Experimental comparison of filter alhorithms for bare-Earth
659   extraction from airborne laser scanning point clouds, *ISPRS Journal of Photogrammetry &*
660   *Remote Sensing*, 59, 85-101.

661 Soares-Frazão, S, Lhomme, J., Guinot, V. and Zech, Y. 2008, Two-dimensional shallow-water
662   model with porosity for urban flood modelling, *Journal of Hydraulic Research*, 46(1), 45-64.

663 Stephens, E.M., Bates, P.D., Freer, J.E. and Mason, D.C., 2012, The impact of uncertainty in
664   satellite data on the assessment of flood inundation models, Journal of Hydrology, 414-415,
665   162-173

666 Tsubaki, R, Fujita, I, and Okabe, T. 2007, Sensitivity of grid spacing to prediction and coherent flow
667   structure of inundation on urbanized area, *32rd Congress of IAHR*, on CD-ROM, Venice, 2007.

668 Tsubaki, R., Nakayama, Y. and Fujita, I., 2008, The design secret of kyokusui-no-en's meandering
669   channel, Journal of Visualization, 11(3), 265-272.

670 Tsubaki, R, and Fujita, I. 2010. Unstructured grid generation using LiDAR data for urban flood
671   modelling, *Hydrological Processes*, 24(11): 1404-1420.

672 Wagner, T., McIntyre, N., Lees, M.J., Wheater, H.S. and Gupta, H.V., 2003, Towards reduced
673   uncertainty in conceptual rainfall-runoff modelling: dynamic identifiably analysis, Hydrological
674   Processes, 17(2), 455-476.

675 Wu, C.L., Chau, K.W. and Li, Y.S., 2009, Methods to improve neural network performance in daily
676   flows prediction, *Journal of Hydrology*, 372(1-4), 80-93.

677 Yu, D. and Lane, S.N., 2005, Urban fluvial flood modelling using a two-dimensional diffusion-wave
678   treatment, part 1: mesh resolution effects, Hydrological Processes, 20(7) 1541-1565,
679   doi:10.1002/hyp.5935.

680

Figure captions
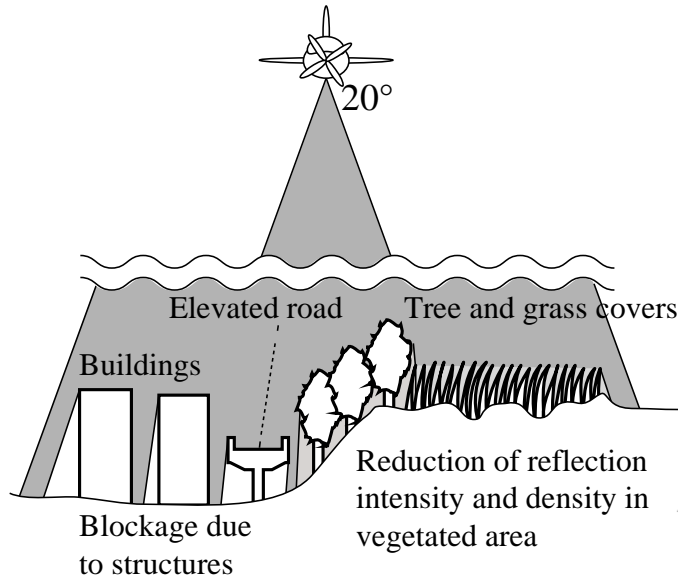
683

684   **Figure 1. Schematic diagram of lase pulse interference in LiDAR survey to detect ground**

685   **surface.**

686

(a) The initial state   (b) The elevation at the center of the square was calculated using the mean of the elevations at the four corners of the square with the addition of the random component.   (c) The elevation at the center of a diamond was calculated using the mean of the elevations at the four corners of the diamonds with the addition of the random component.   (d) The square to diamond calculation

687

688   **Figure 2. The diamond-square algorithm for fractal topography generation.**

689

(a) ErrorA   (b) ErrorB   (c) ErrorC
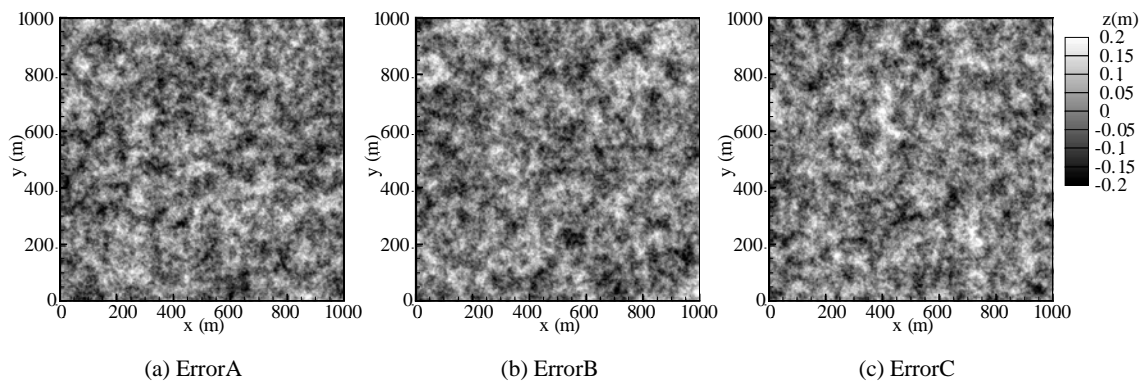
Figure 3**. The generated fractal topography representing LiDAR measurement error. The magnitude of the elevation fluctuation was set as $\sigma = 0.075$ m.**
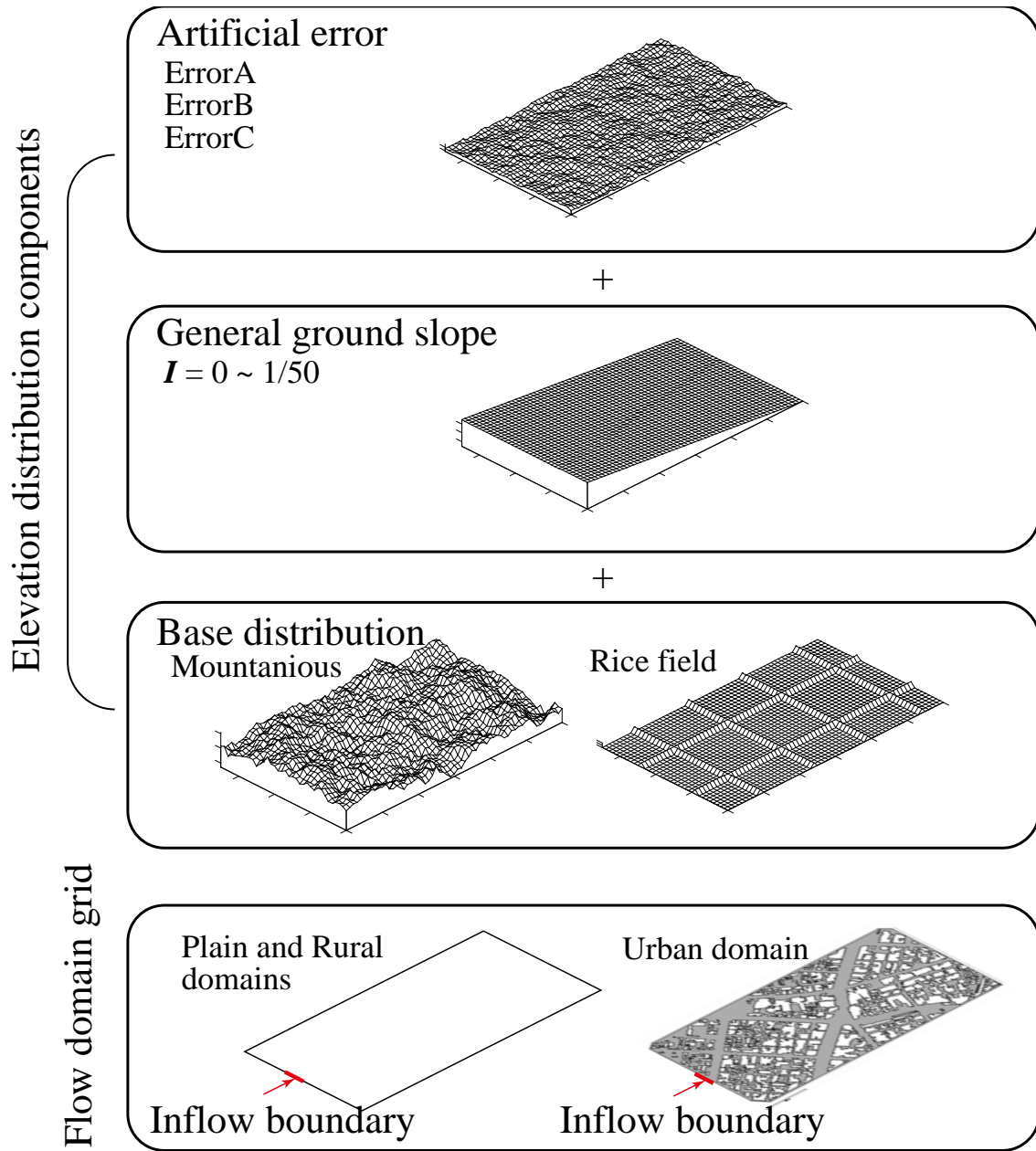
Figure 4**. A schematic of the topographical data set generation. Topographical data consists of a gridded flow domain and an elevation distribution. For urban topography, an arrangement of buildings is represented in the grid. The elevation distribution, consisting of the base distribution, differs with each topographical case, the general ground slope, and the artificial elevation error.**
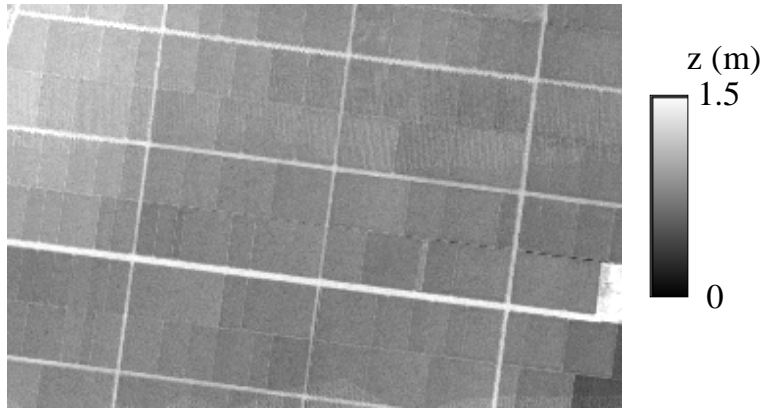
100 m

Figure 5. The base distribution used for the rural topography. The elevation distribution was obtained from an actual LiDAR survey while measuring a rice field in Niigata, Japan.

200 m

Figure 6. The flow domain boundary utilized for urban topography. The topography was obtained from an actual LiDAR survey of the city of Hyogo, Japan. In this work, a building area was treated as an impermeable wall during inundation simulations.

710
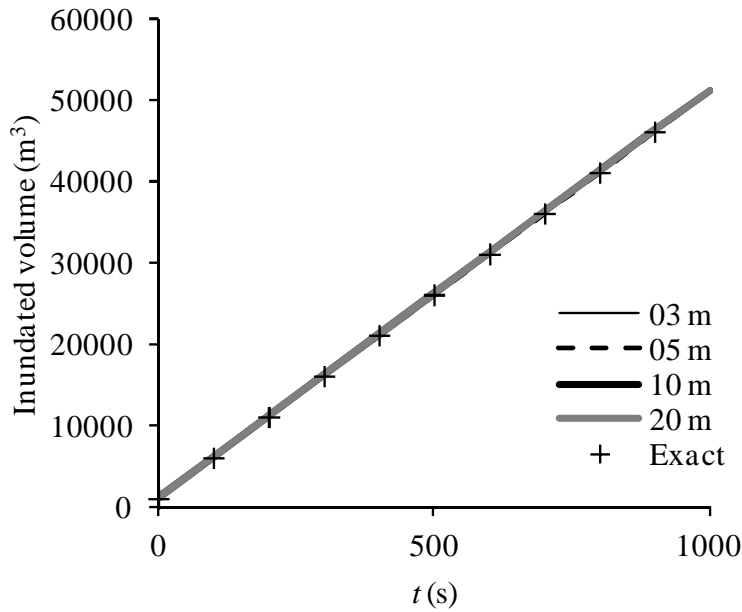
Figure 7**. The time-series of water volume in the calculation domain for the Plain case with *I* =**

1/2000. The calculated results of the four grid sizes and the exact value are compared.

713

(a) I=1/300

(b) I=1/50

714
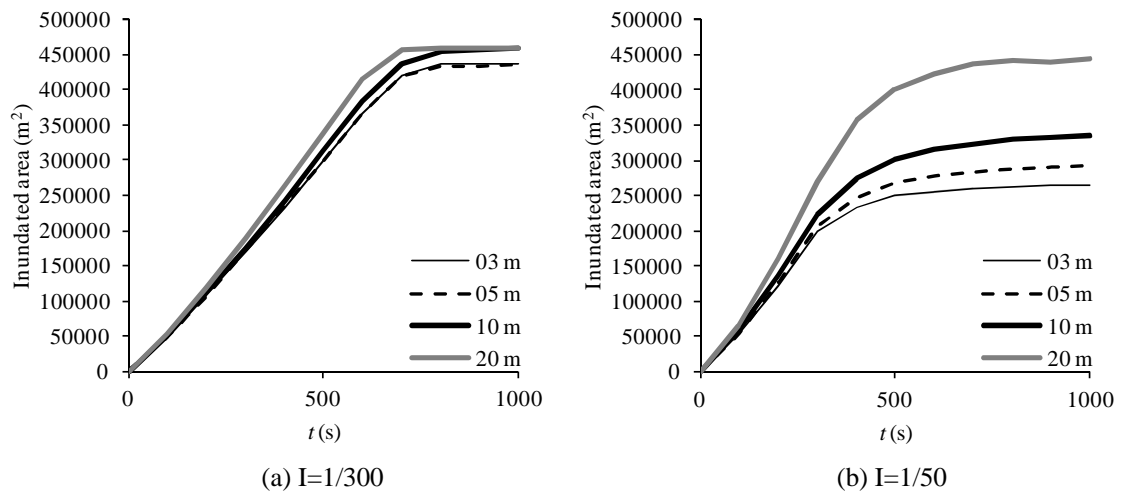
Figure 8**. Hydrographs of the inundated area. The left figure and the right figure compare the**

results of the four grid sizes in a medium bed slope (*I* = 1/300) and a steep bed slope (*I* = 1/50),

respectively.

718

$t = 200$ s

200 m
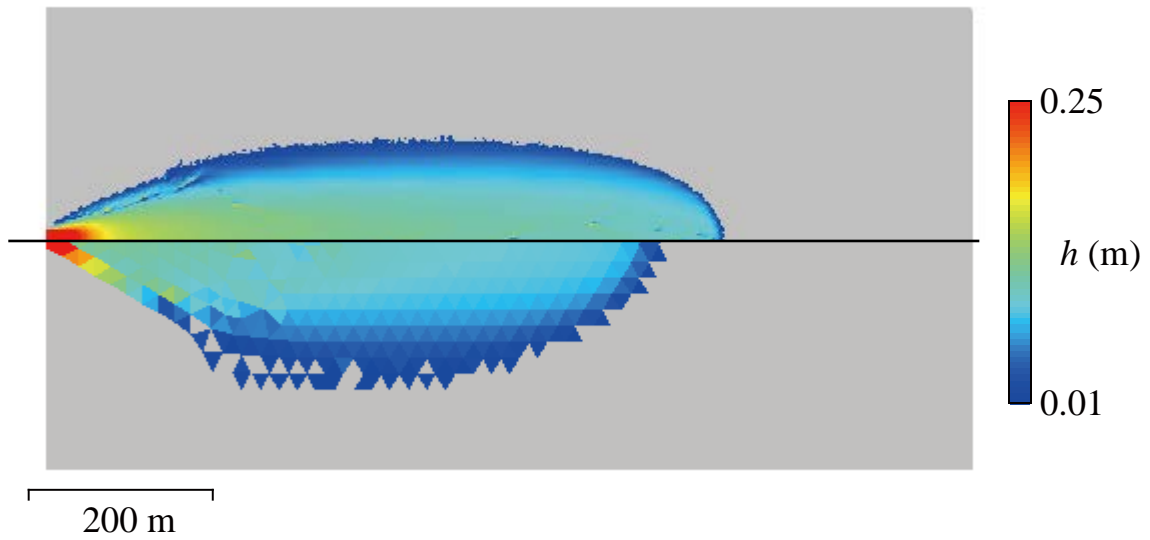
Figure 9. A snap shot of the inundated water depth, h, at $t = 200$ s for a steep bed slope ($I =$ 1/50) case. The upper half represents a small grid (the grid size is 3 m) result and the lower half provides a coarse grid (the 20 m in the grid size) result. The hatched areas indicate a dry region.
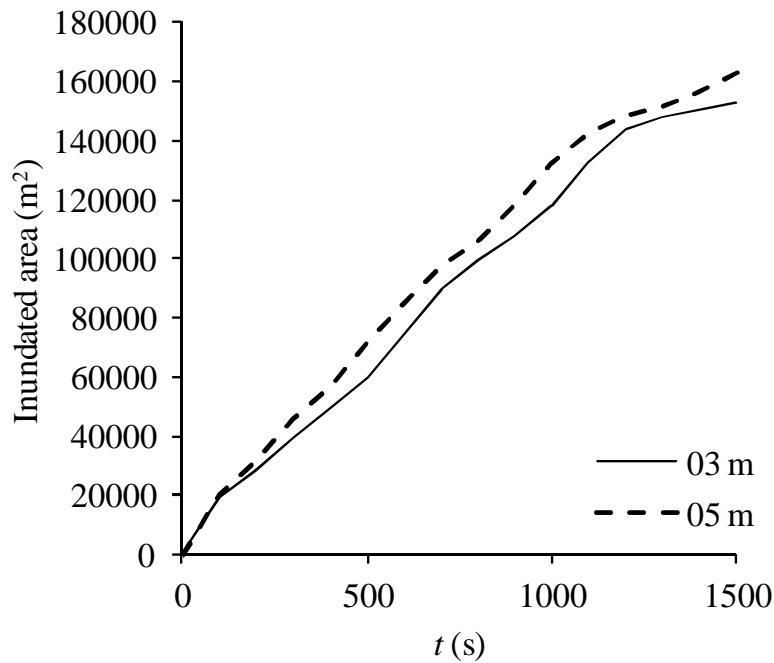
Figure 10. The time series of the inundated area calculated using the two grid sizes.

728
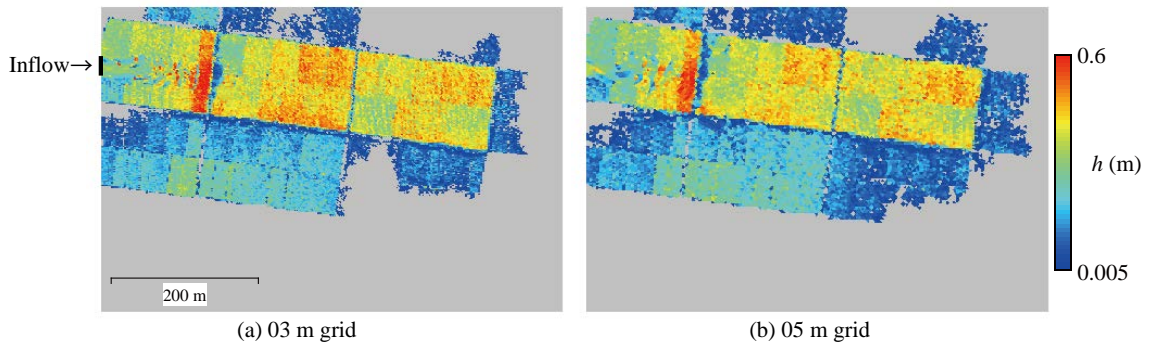
Figure 11**. A snap shot of water depth at** *t* **= 1000 s, calculated using two grid sizes.**

730

731
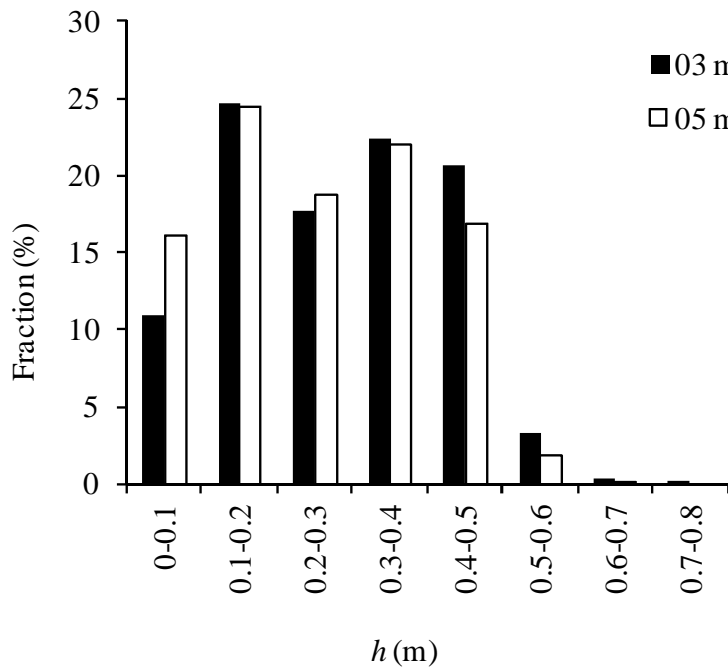
Figure 12**. A percentile distribution of the water depth distribution at** *t* **= 1000 s.**

733

734
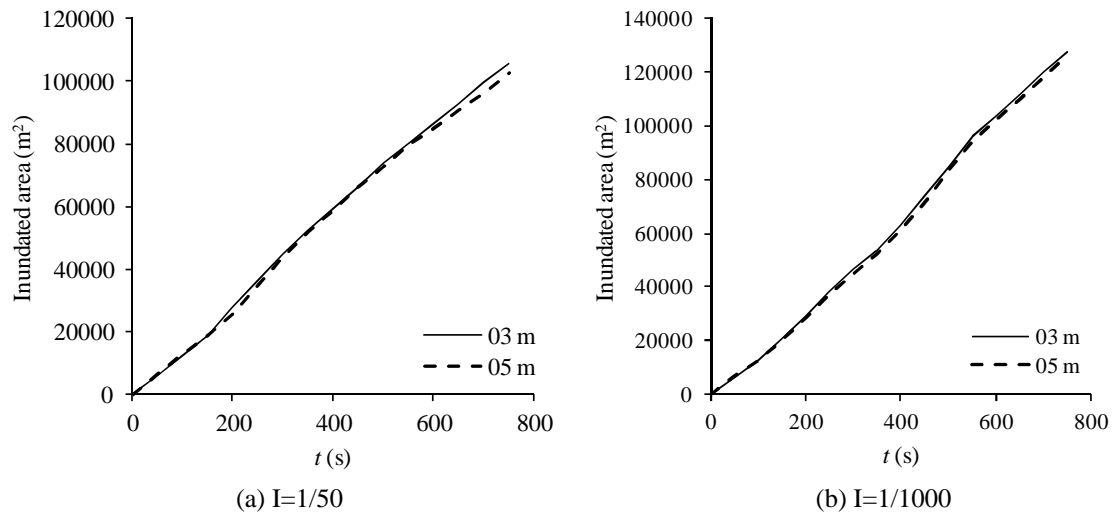
735 **Figure** 13**. A time series of the inundated area for steep (left side sub-figure) and mild sloped**

736 **(right side sub-figure) urban topographies, calculated using two grid sizes.**

737

738
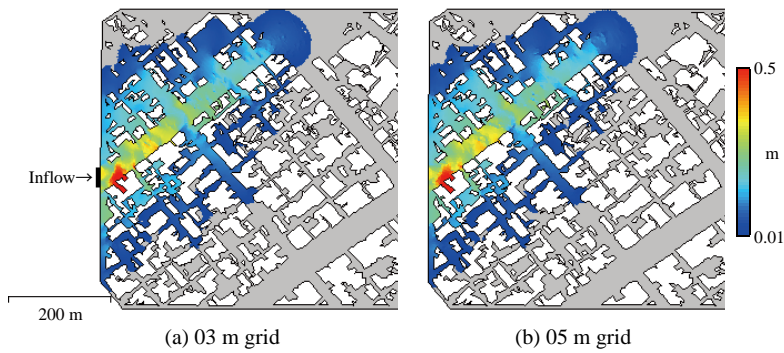
739 **Figure** 14**. A snap shot of the inundated water depth at t = 400 s, for the mild bed slope (I =**

740 **1/1000) case.**

741

742
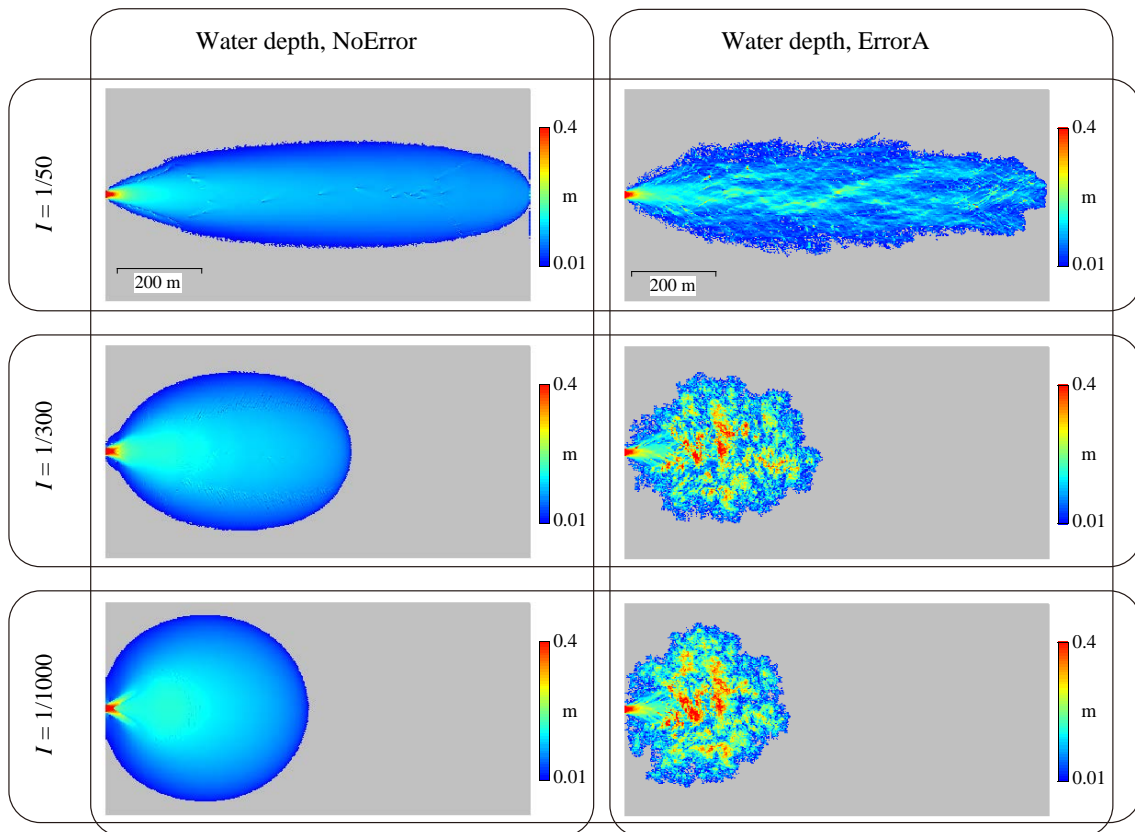
Figure 15**. A comparison of the general bed slope effect and the elevation noise; the left-hand side indicates no-additional-noise result; the right-hand side provides an additional noise A pattern. A snap shot is depicted at *t* = 300 s.**

746

747
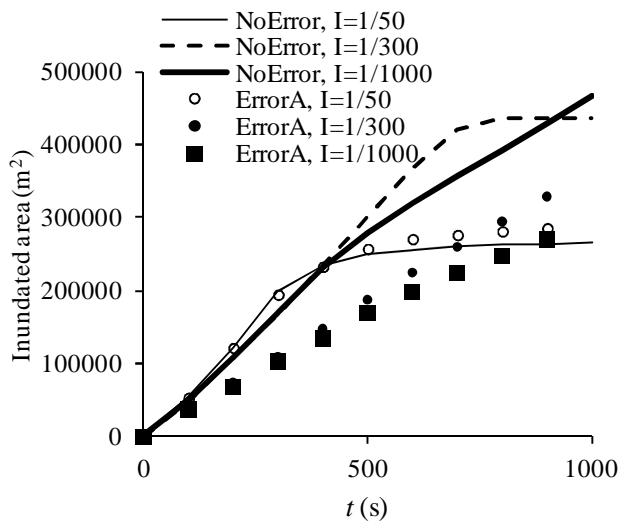
Figure 16. The time series of the inundated area for Plain topographies with and without elevation error and for different ground slopes.

750

751
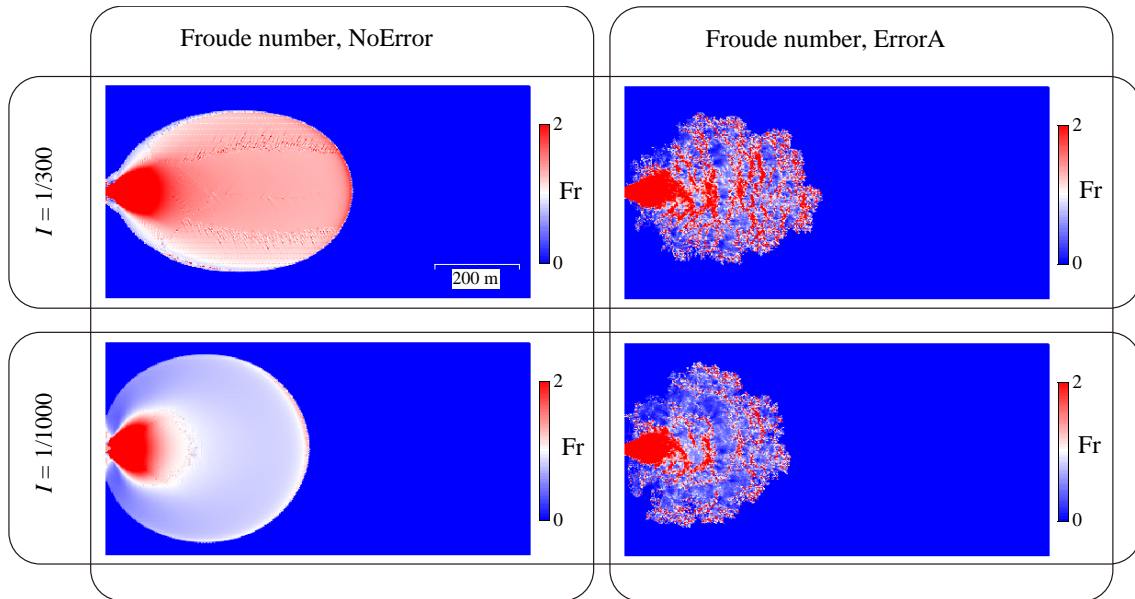
Figure 17**. A comparison of the Froude number distributions of the results calculated with and without elevation error. A snap shot at** t **= 300 s is shown.**

754

(a) 03m grid, NoError   (b) 05m grid, NoError

(c) 03m grid, ErrorA   (d) 03m grid, ErrorB
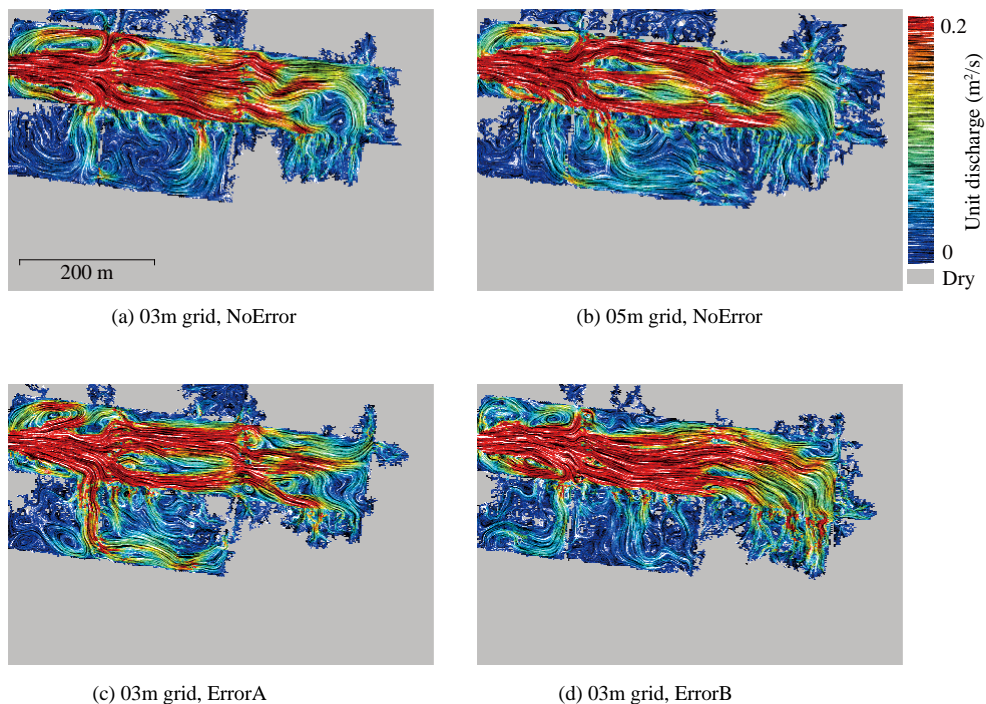
Figure 18**. A comparison of the flow structure at** t **= 1000 s, calculated using different grid sizes and different error patterns. Images were generated using the LIC (Line Integral Convolution) method. The direction of texture indicates the local flow direction. The density of the texture corresponds to the local discharge per unit width.**

760

761
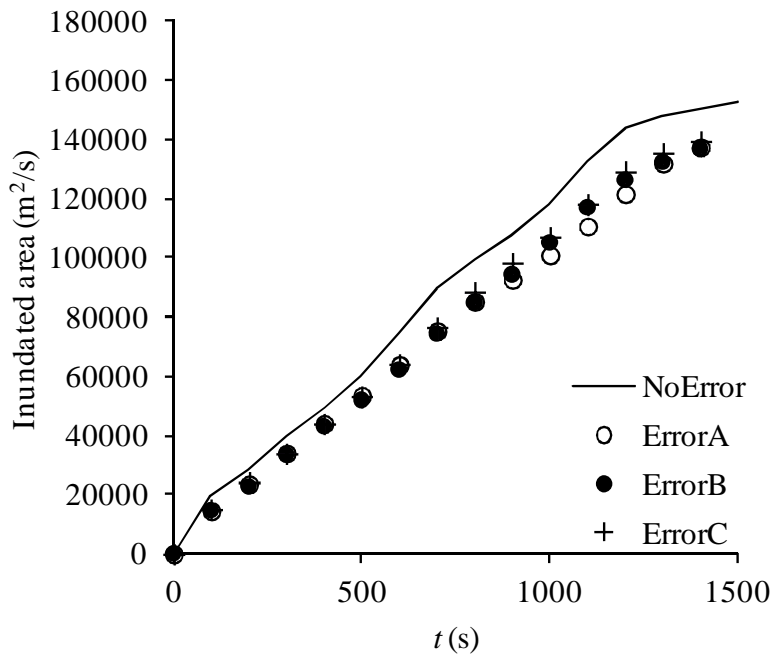
Figure 19**. A time series of the inundated area for Rural topographies with and without**
elevation error. The grid size is 03 m.

764

765
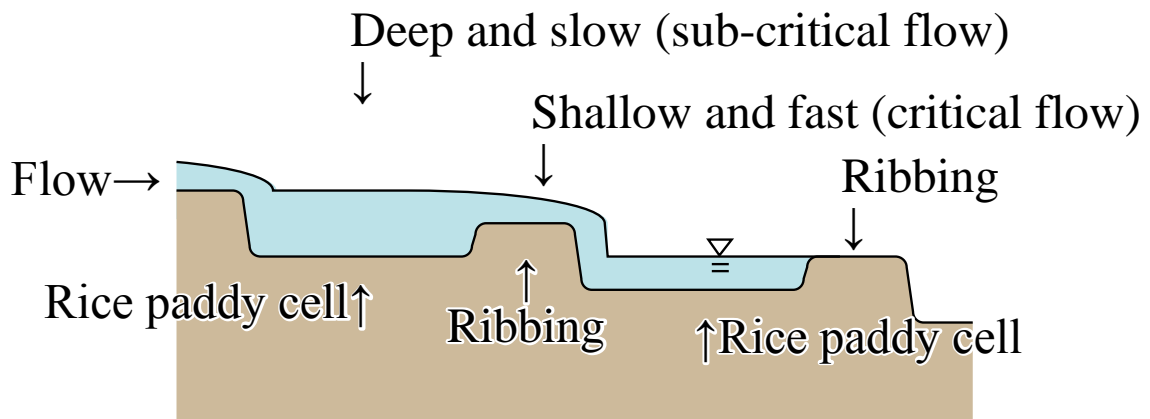
Figure 20**. A schematic diagram, vertical section, of the structure of inundation flow and its**
relationship to topography in Rural areas.

768
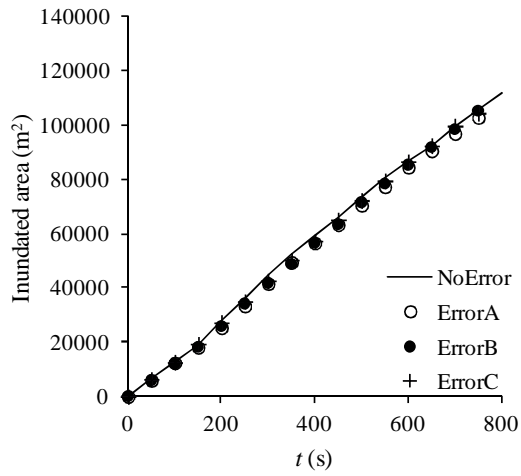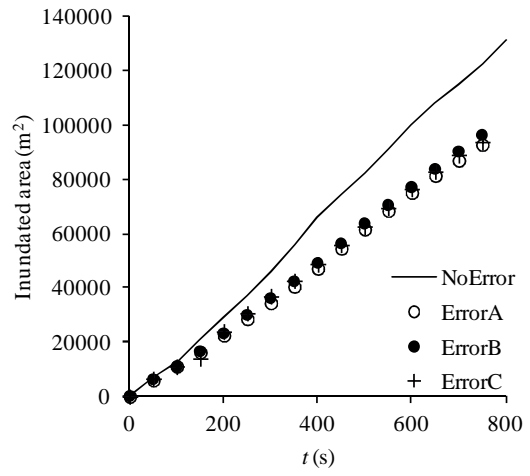
769

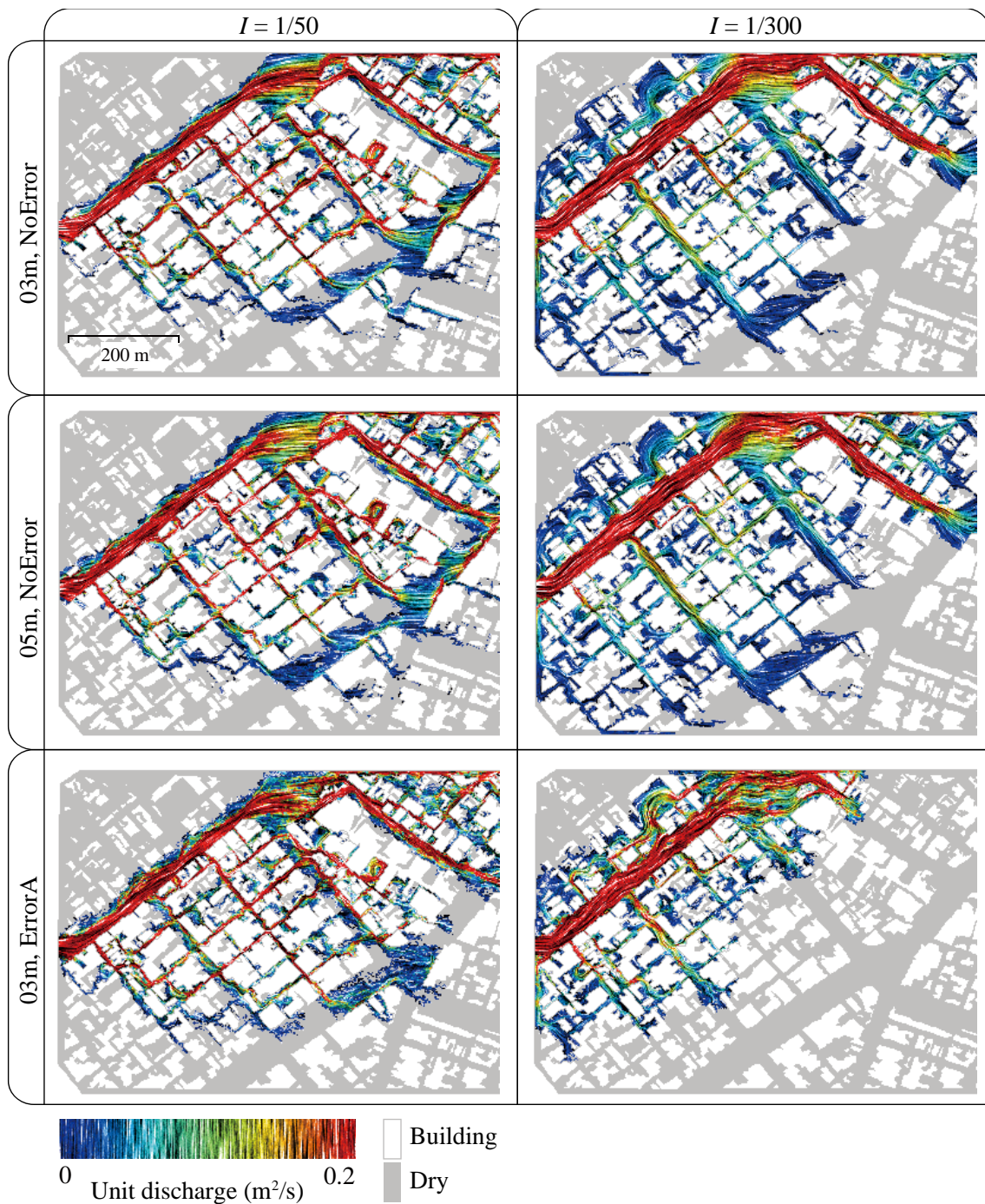770   **Figure** 21**. A time series of the inundated area of Urban topographies for a steep slope (I =**

771   **1/50) and a medium slope (I = 1/300) with and without elevation error. The grid size is 03 m.**

772

773
774 **Figure 22. LIC images of urban topography cases calculated using different conditions at $t =$**
775 **800 s. The upper row provides the results calculated using a 03 m grid size without elevation**
776 **error. The medium row provides results obtained using a 05 m grid without error. The lower**
777 **row depicts results with a 03 m grid that contained elevation error. The left column provides**
778 **the results of a steep slope ($I = 1/50$), and the right column provides the results of a medium**
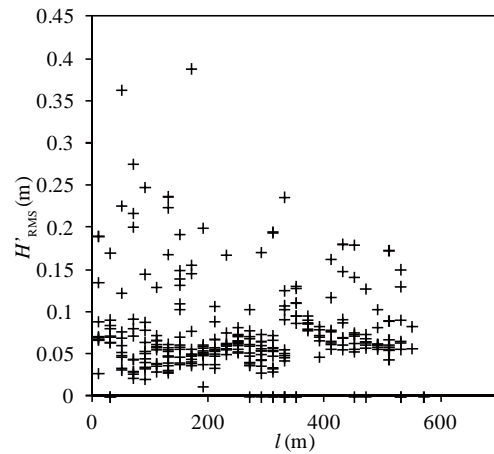779 **slope ($I = 1/300$).**
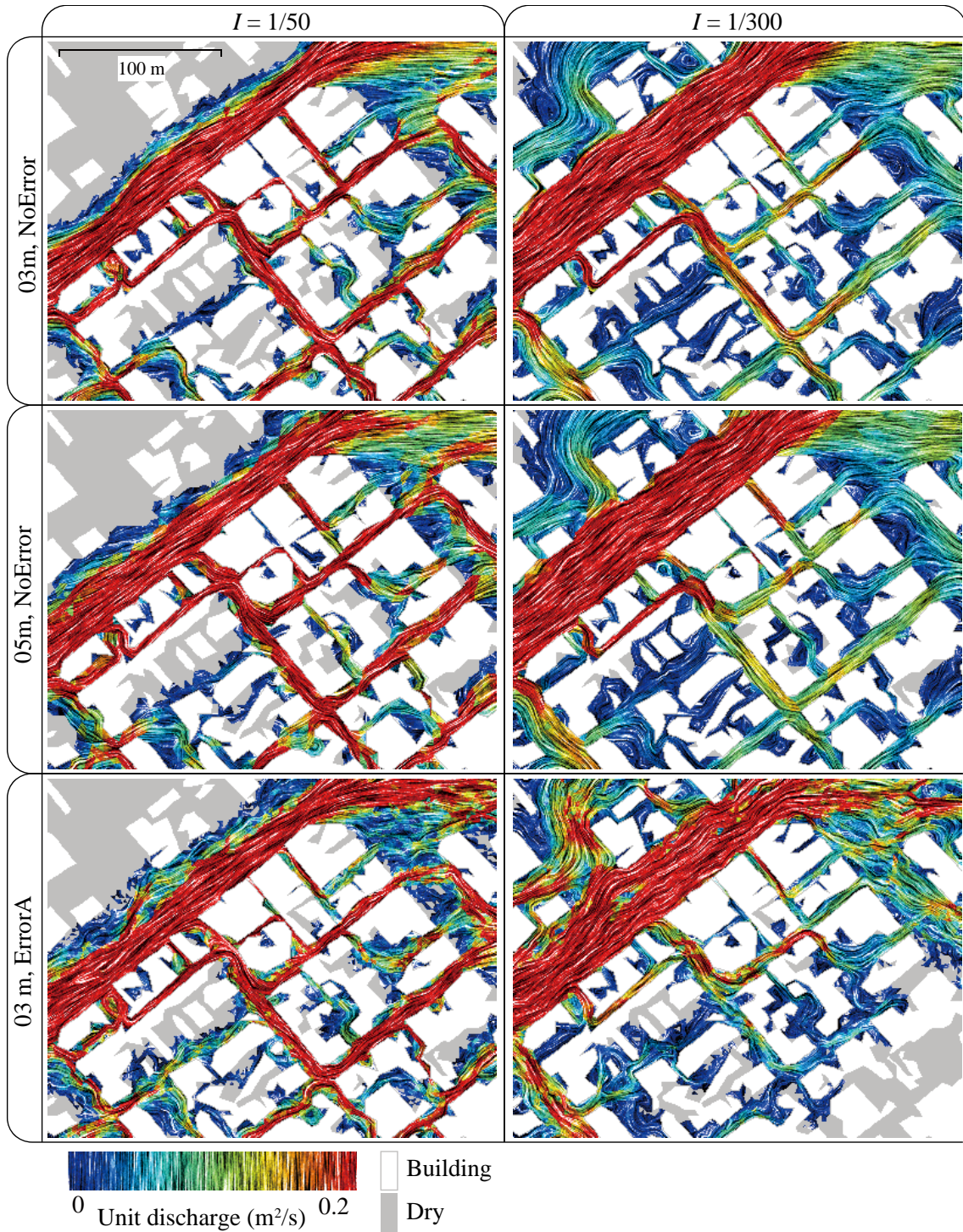
Figure 23. A close up of the inflow area of LIC images. The calculated conditions and the arrangement of the sub-figures are identical to those provided in Figure 21.
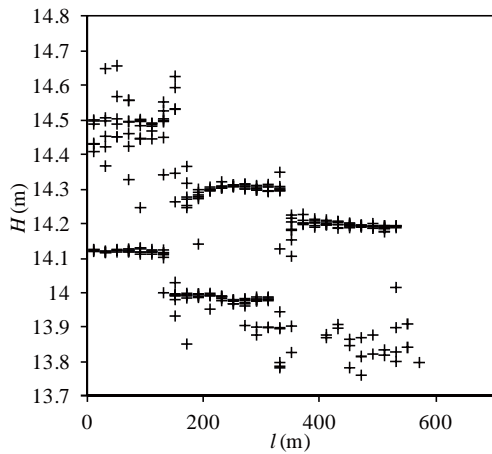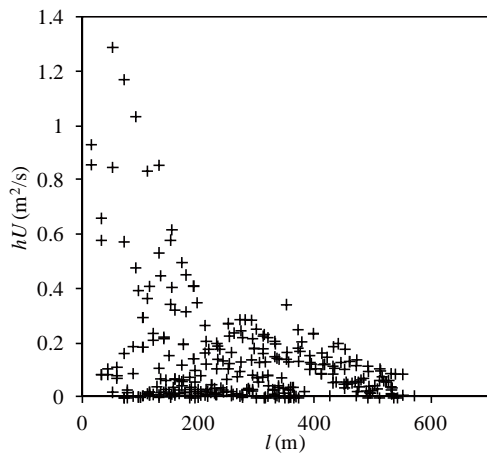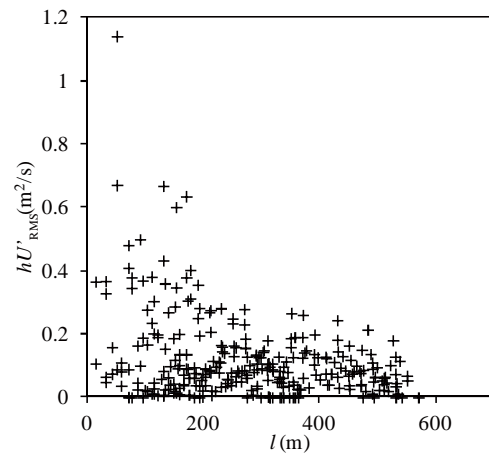
(a) Water stage of 03m-NoError case

(b) Root mean square of water stage

(c) Unit discharge of 03m-NoError case
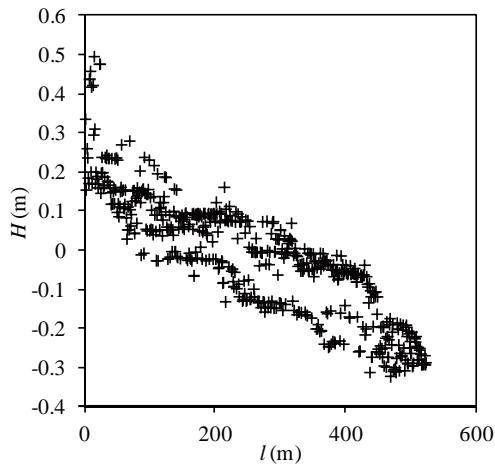
(d) Root mean square of unit discharge

785

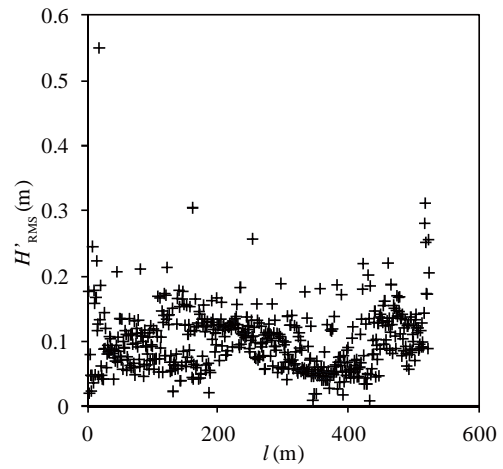786 **Figure** 24. **The relationship between distance from the inflow point and the flow parameters,**

787 **and errors at t = 1000 s for the Rural case. Sub-figures (a) and (c) display the distributions of**

788 **the water stage and the unit width discharge of the base calculation (03 m-NoError).**

789 **Sub-figures (b) and (d) depict the water stage and the unit width discharge errors calculated**

790 **using the standard deviation error for the three elevation noise cases.**

791

(a) Water stage of 03m-NoError case

(b) Root mean square of water stage errors

(c) Unit discharge of 03m-NoError case
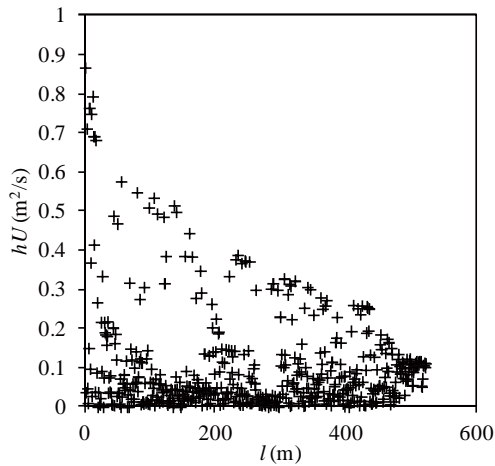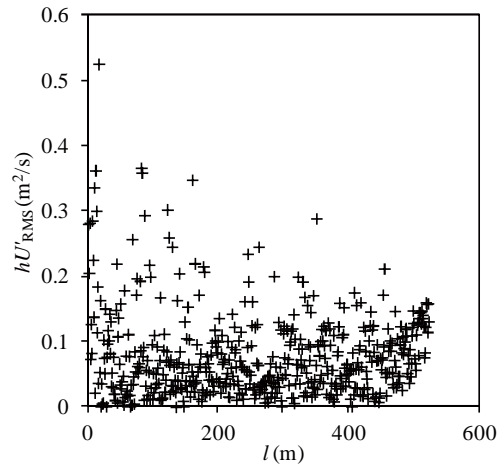
(d) Root mean square of unit discharge errors

792

793 **Figure** 25**. The relationship between distance from the inflow point and flow parameters, and**

794 **those errors at** t **= 800 s for the Urban case of** I **= 1/1000. Sub-figures (a) and (b) provide the**

795 **distributions of the water stage and the discharge par unit width of the base calculation**

796 **(03m-NoError). Sub-figures (c) and (d) depict the water stage and the unit discharge errors**

797 **calculated using the standard deviation error for the three elevation noise cases.**

798

799

800

801

802

803

804

Table captions

Table 1. The calculation case list

Topographical type	Additional slope I	Error pattern			
		No	A	B	C
Plain	1/2000	3, 5, 10, 20	3		
	1/1000	3, 5, 10, 20	3		
	1/300	3, 5, 10, 20	3, 5, 10, 20	3	3
	1/50	3, 5, 10, 20	3, 5, 10, 20		
Rural	0	3, 5	3, 5	3, 5	3, 5
	1/1000	3, 5			3, 5
	1/300	3, 5			3, 5
	1/50	3, 5			3, 5
Urban	1/1000	3, 5	3, 5	3, 5	3, 5
	1/300	3, 5	3, 5	3, 5	3, 5
	1/50	3, 5	3, 5	3, 5	3, 5

Number in thick box indicates the grid size of calculated case

Table 2. The standard deviations between local flow parameters at $t = 300$ s for the Plain case,
$I = 1/300$. The result of the 03 m, NoError case is assumed to be a benchmark; and the
difference between the 03m, No error case, and each case is indicated as a standard deviation.

		σ_z (m)	σ_h (m)	σ_H (m)	σ_{hU} (m^2/s)	σ_{hUU} (m^3/s^2)
05m	NoError	0.0012	0.0054	0.0081	0.018	0.133
10m	NoError	0.0022	0.0134	0.0124	0.041	0.356
03m	ErrorA	0.0648	0.0619	0.0736	0.101	0.403
03m	ErrorB	0.0595	0.0589	0.0796	0.081	0.322
03m	ErrorC	0.0628	0.0607	0.0813	0.104	0.418

$n \geqq 282$

Table 3. The standard deviations between local flow parameters at t = 1000 s for the Rural
case. The data was processed using the method in Table 2.

		σ_z (m)	σ_h (m)	σ_H (m)	σ_{hU} (m^2/s)	σ_{hUU} (m^3/s^2)
05m	NoError	0.0333	0.0429	0.0589	0.112	0.241
03m	ErrorA	0.0659	0.0735	0.0552	0.104	0.190
03m	ErrorB	0.0638	0.0696	0.0538	0.087	0.159
03m	ErrorC	0.0675	0.0674	0.0543	0.114	0.272

$n \geqq 283$

822 **Table 4. Standard deviations between local flow parameters at t = 500 s for the Urban case, I =**

823 **1/1000. The data was processed using methods from Table 2.**

824

		σ_z (m)	σ_h (m)	σ_H (m)	σ_{hU} (m^2/s)	σ_{hUU} (m^3/s^2)
05m	NoError	0.0013	0.0141	0.0407	0.029	0.027
03m	ErrorA	0.0678	0.0661	0.0663	0.056	0.103
03m	ErrorB	0.0665	0.0636	0.0702	0.070	0.146
03m	ErrorC	0.0641	0.0636	0.0741	0.051	0.131

$n \geqq 228$

825
826